

The Sloan Digital Sky Survey Quasar Catalog: Fourteenth data release[★]

Isabelle Pâris¹, Patrick Petitjean², Éric Aubourg³, Adam D. Myers⁴, Alina Streblyanska^{5,6}, Brad W. Lyke⁴, Scott F. Anderson⁷, Éric Armengaud⁸, Julian Bautista⁹, Michael R. Blanton¹⁰, Michael Blomqvist¹, Jonathan Brinkmann¹¹, Joel R. Brownstein⁹, William Nielsen Brandt^{12,13,14}, Étienne Burtin⁸, Kyle Dawson⁹, Sylvain de la Torre¹, Antonis Georgakakis¹⁵, Héctor Gil-Marín^{16,17}, Paul J. Green¹⁸, Patrick B. Hall¹⁹, Jean-Paul Kneib²⁰, Stephanie M. LaMassa²¹, Jean-Marc Le Goff⁸, Chelsea MacLeod¹⁸, Vivek Mariappan⁹, Ian D. McGreer²², Andrea Merloni¹⁵, Pasquier Noterdaeme², Nathalie Palanque-Delabrouille⁸, Will J. Percival²³, Ashley J. Ross²⁴, Graziano Rossi²⁵, Donald P. Schneider^{12,13}, Hee-Jong Seo²⁶, Rita Tojeiro²⁷, Benjamin A. Weaver²⁸, Anne-Marie Weijmans²⁷, Christophe Yèche⁸, Pauline Zarrouk⁸, and Gong-Bo Zhao^{29,23}

(Affiliations can be found after the references)

Received 10 December 2017 / Accepted 14 January 2018

ABSTRACT

We present the data release 14 Quasar catalog (DR14Q) from the extended Baryon Oscillation Spectroscopic Survey (eBOSS) of the Sloan Digital Sky Survey IV (SDSS-IV). This catalog includes all SDSS-IV/eBOSS objects that were spectroscopically targeted as quasar candidates and that are confirmed as quasars via a new automated procedure combined with a partial visual inspection of spectra, have luminosities $M_i [z = 2] < -20.5$ (in a Λ CDM cosmology with $H_0 = 70 \text{ km s}^{-1} \text{ Mpc}^{-1}$, $\Omega_M = 0.3$, and $\Omega_\Lambda = 0.7$), and either display at least one emission line with a full width at half maximum larger than 500 km s^{-1} or, if not, have interesting/complex absorption features. The catalog also includes previously spectroscopically-confirmed quasars from SDSS-I, II, and III. The catalog contains 526 356 quasars (144 046 are new discoveries since the beginning of SDSS-IV) detected over 9376 deg^2 (2044 deg^2 having new spectroscopic data available) with robust identification and redshift measured by a combination of principal component eigenspectra. The catalog is estimated to have about 0.5% contamination. Redshifts are provided for the Mg II emission line. The catalog identifies 21 877 broad absorption line quasars and lists their characteristics. For each object, the catalog presents five-band (u, g, r, i, z) CCD-based photometry with typical accuracy of 0.03 mag. The catalog also contains X-ray, ultraviolet, near-infrared, and radio emission properties of the quasars, when available, from other large-area surveys. The calibrated digital spectra, covering the wavelength region $3610\text{--}10\,140 \text{ \AA}$ at a spectral resolution in the range $1300 < R < 2500$, can be retrieved from the SDSS Science Archiver Server.

Key words. catalogs – surveys – quasars: general

1. Introduction

Since the identification of the first quasar redshift by Schmidt (1963), each generation of spectroscopic surveys has enlarged the number of known quasars by roughly an order of magnitude: the Bright Quasar Survey (Schmidt & Green 1983) reached the 100 discoveries milestone, followed by the Large Bright Quasar Survey (LBQS; Hewett et al. 1995) and its 1000 objects, then the $\sim 25\,000$ quasars from the 2dF Quasar Redshift Survey (2QZ; Croom et al. 2004), and the Sloan Digital Sky Survey (SDSS; York et al. 2000) with over 100 000 new quasars (Schneider et al. 2010). Many other surveys have also significantly contributed to increase the number of known quasars (e.g. Osmer & Smith 1980; Boyle et al. 1988; Storrie-Lombardi et al. 1996).

Each iteration of SDSS has pursued different science goals, and hence set different requirements for their associated quasar target selection.

SDSS-I/II (York et al. 2000) aimed to observe $\sim 10^5$ quasars; The final quasar list was presented in the SDSS data release 7

(DR7) quasar catalog (Schneider et al. 2010). The main science driver was studies of the quasar population through the measurement of their luminosity function (e.g. Richards et al. 2006) and clustering properties (e.g. Hennawi et al. 2006; Shen et al. 2007). The quasar program of SDSS-I/II also led to the discovery of a significant sample of $z > 5$ quasars (e.g. Fan et al. 2006; Jiang et al. 2008), large samples of broad absorption line (BAL) quasars (e.g. Reichard et al. 2003; Trump et al. 2006; Gibson et al. 2008), type 2 candidates (Reyes et al. 2008) or samples of objects with peculiar properties such as weak emission lines (Diamond-Stanic et al. 2009). Quasar target selection algorithms for SDSS-I/II are fully detailed in Richards et al. (2002) and Schneider et al. (2010).

The main motivation to observe quasars with SDSS-III/BOSS (Eisenstein et al. 2011; Dawson et al. 2013) was to constrain the Baryon Acoustic Oscillation (BAO) scale at $z \sim 2.5$ using the H I located in the intergalactic medium (IGM) as a tracer of large scale structures. About 270 000 quasars, mostly in the redshift range 2.15–3.5 for which at least part of the Lyman- α forest lies in the spectral range, have been discovered by SDSS-III/BOSS. The measurement of the auto-correlation

[★] http://www.sdss.org/dr14/algorithms/qso_catalog

function of the Lyman- α forest (e.g. [Bautista et al. 2017](#)) and the cross-correlation of quasars and the Lyman- α forest (e.g. [du Mas des Bourboux et al. 2017](#)) have provided unprecedented cosmological constraints at $z \sim 2.5$. This sample was also used to study the luminosity function of quasars ([Ross et al. 2013](#); [Palanque-Delabrouille et al. 2013](#)), moderate-scale clustering of $z \sim 2.5$ quasars (e.g. [Eftekharzadeh et al. 2015](#)). Repeat spectroscopic observations of BAL quasars have been performed to constrain the scale and dynamics of quasar outflows ([Filiz Ak et al. 2012, 2013, 2014](#)). Peculiar population of quasars have been also identified in this enormous sample such as $z > 2$ type 2 quasar candidates ([Alexandroff et al. 2013](#)) or extremely red quasars ([Ross et al. 2015](#); [Hamann et al. 2017](#)). In order to maximize the number of $z > 2$ quasars, the target selection for SDSS-III/BOSS used a variety of target selection algorithms ([Bovy et al. 2011, 2012](#); [Kirkpatrick et al. 2011](#); [Yèche et al. 2010](#); [Palanque-Delabrouille et al. 2011](#); [Richards et al. 2004](#)). The overall quasar target selection strategy is described in [Ross et al. \(2012\)](#).

Quasar observation in SDSS-IV is driven by multiple scientific goals such as cosmology, understanding the physical nature of X-ray sources and variable sources.

SDSS-IV/eBOSS aims to constrain the angular-diameter distance $d_A(z)$ and the Hubble parameter $H(z)$ in the redshift range 0.6–3.5 using four different tracers of the underlying density field over 7500 deg²: 250 000 new luminous red galaxies (LRG) at $0.6 < z < 1.0$, 195 000 new emission line galaxies (ELG) at $0.7 < z < 1.1$, 450 000 new quasars at $0.9 < z < 2.2$, and the Lyman- α forest of 60 000 new $z > 2.2$ quasars.

SDSS-IV/SPIDERS (SPectroscopic IDentification of ERosita Sources) investigates the nature of X-ray emitting sources, including active galactic nuclei ([Dwelly et al. 2017](#)) and galaxy clusters ([Clerc et al. 2016](#)). Initially, SPIDERS targets X-ray sources detected mainly in the ROSAT All Sky Survey ([Voges et al. 1999, 2000](#)) which has recently been reprocessed ([Boller et al. 2016](#)). In late 2018, SPIDERS plans to begin targeting sources from the eROSITA instrument on board the Spectrum Roentgen Gamma satellite ([Predehl et al. 2010](#); [Merloni et al. 2012](#)). About 5% of eBOSS fibers are allocated to SPIDERS targets. A total of 22 000 spectra of active galactic nuclei are expected by the end of the survey, about 5000 of them being also targeted by SDSS-IV/eBOSS.

Finally, SDSS-IV/TDSS (Time Domain Spectroscopic Survey) that aims to characterize the physical nature of time-variable sources, primarily on sources detected to be variable in Pan-STARRS1 data (PS1; [Kaiser et al. 2010](#)) or between SDSS and PS1 imaging, has been allocated about 5% of eBOSS fibers ([Morganson et al. 2015](#); [MacLeod et al. 2017](#)). The targets identified in PS1 are a mix of quasars (about 60%) and stellar variables (about 40%). It will lead to the observation of about 120 000 quasars with a majority of them also targeted by SDSS-IV/eBOSS.

This paper presents the SDSS-IV/eBOSS quasar catalog, denoted DR14Q, that compiles all the spectroscopically-confirmed quasars identified in the course of any of the SDSS iterations and released as part of the SDSS Fourteenth data release ([Abolfathi et al. 2017](#)). The bulk of the newly discovered quasars contained in DR14Q arise from the main SDSS-IV/eBOSS quasar target selection ([Myers et al. 2015](#)). The rest were observed by ancillary programs (83 430 quasars not targeted by the SDSS-IV/eBOSS main quasar survey; see [Dawson et al. 2013](#); [Ahn et al. 2014](#); [Alam et al. 2015](#)), and TDSS and SPIDERS (27 547 and 1090, respectively).

We summarize the target selection and observations in Sect. 2. We describe the visual inspection process and describe the definition of the DR14Q parent sample in Sect. 3. We discuss the accuracy of redshift estimates in Sect. 4 and present our automated detection of BAL quasars in Sect. 5. General properties of the DR14Q sample are reviewed in Sects. 6 and 7, and the format of the catalog is described in Sect. 8. Finally, we conclude in Sect. 9.

In the following, we use a Λ CDM cosmology with $H_0 = 70 \text{ km s}^{-1} \text{ Mpc}^{-1}$, $\Omega_M = 0.3$, $\Omega_\Lambda = 0.7$ ([Spergel et al. 2003](#)). We define a quasar as an object with a luminosity $M_i[z = 2] < -20.5$ and either displaying at least one emission line with a full-width at half maximum (FWHM) $> 500 \text{ km s}^{-1}$ or, if not, having interesting/complex absorption features. Indeed, a few tens of objects have weak emission lines but the Lyman- α forest is clearly visible in their spectra ([Diamond-Stanic et al. 2009](#)), and thus they are included in the DR14Q catalog. About 200 quasars with unusual BALs are also included in our catalog ([Hall et al. 2002](#)) even though they do not formally meet the requirement on emission-line width. All magnitudes quoted here are point spread function (PSF) magnitudes ([Stoughton et al. 2002](#)) and are corrected for Galactic extinction ([Schlafly & Finkbeiner 2011](#)).

2. Survey outline

In this section, we focus on imaging data used to perform the target selection of SDSS-IV quasar programs and new spectroscopic data obtained since August 2014.

2.1. Imaging data

Three sources of imaging data have been used to target quasars in SDSS-IV/eBOSS (full details can be found in [Myers et al. 2015](#)): updated calibrations of SDSS imaging, the Wide-Field Infrared Survey (WISE; [Wright et al. 2010](#)), and the Palomar Transient Factory (PTF; [Rau et al. 2009](#); [Law et al. 2009](#)).

SDSS imaging data were gathered using the 2.5 m wide-field Sloan telescope ([Gunn et al. 2006](#)) to collect light for a camera with $30 \text{ 2k} \times \text{2k}$ CCDs ([Gunn et al. 1998](#)) over five broad bands – *ugriz* ([Fukugita et al. 1996](#)). A total of 14 555 unique square degrees of the sky were imaged by this camera, including contiguous areas of $\sim 7500 \text{ deg}^2$ in the North Galactic Cap (NGC) and $\sim 3100 \text{ deg}^2$ in the SGC that comprise the uniform “Legacy” areas of the SDSS ([Aihara et al. 2011](#)). These data were acquired on dark photometric nights of good seeing ([Hogg et al. 2001](#)). Objects were detected and their properties were measured by the photometric pipeline ([Lupton et al. 2001](#); [Stoughton et al. 2002](#)) and calibrated photometrically ([Smith et al. 2002](#); [Ivezić et al. 2004](#); [Tucker et al. 2006](#); [Padmanabhan et al. 2008](#)), and astrometrically ([Pier et al. 2003](#)). Targeting for eBOSS is conducted using SDSS imaging that is calibrated to the [Schlafly et al. \(2012\)](#) Pan-STARRS solution ([Finkbeiner et al. 2016](#)). These imaging data were publicly released as part of SDSS-DR13 ([Albaret et al. 2016](#)).

The quasar target selection for SDSS-IV/eBOSS also makes use of the W1 and W2 WISE bands centered on 3.4 and 4.6 μm . The “unWISE” coadded photometry is applied to sources detected in the SDSS imaging data as described in [Lang \(2014\)](#). This approach produces photometry of custom coadds of the WISE imaging at the position of all SDSS primary sources.

Imaging data from PTF is also used to target quasars using variability in SDSS-IV/eBOSS. Starting from the individual

calibrated frames available from IPAC (Infrared Processing & Analysis Center; Laher et al. 2014), a customized pipeline is applied to build coadded PTF images on a timescale adapted to quasar targeting, i.e. typically 1–4 epochs per year, depending on the cadence and total exposure time within each field. A stack of all PTF imaging epochs is also constructed to create a catalog of PTF sources. Finally, light curves are created using coadded PTF images to perform the selection of quasar candidates.

2.2. Target selection

In order to achieve a precision of 2.8% on $d_A(z)$ and 4.2% on $H(z)$ measurement with the quasar sample, it is necessary to achieve a surface density of at least 58 quasars with $0.9 < z < 2.2$ per square degree (Dawson et al. 2016). The SDSS-IV/eBOSS “CORE” sample is intended to recover sufficient quasars in this specific redshift range and additional quasars at $z > 2.2$ to supplement SDSS-III/BOSS. The CORE sample homogeneously targets quasars at all redshifts $z > 0.9$ based on the XDQSOz method (Bovy et al. 2012) in the optical and a WISE-optical color cut. To be selected, it is required that point sources have a XDQSOz probability to be a $z > 0.9$ quasar larger than 0.2 and pass the color cut $m_{\text{opt}} - m_{\text{WISE}} \geq (g - i) + 3$, where m_{opt} is a weighted stacked magnitude in the g , r and i bands and m_{WISE} is a weighted stacked magnitude in the W1 and W2 bands. Quasar candidates have $g < 22$ or $r < 22$ with a surface density of confirmed new quasars (at any redshifts) of $\sim 70 \text{ deg}^{-2}$.

SDSS-IV/eBOSS also selects quasar candidates over a wide range of redshifts using their photometric variability measured from the PTF. In the following we refer to this sample as the “PTF” sample. These targets have $r > 19$ and $g < 22.5$ and provide an additional 3–4 $z > 2.1$ quasars per deg^2 .

In addition, known quasars with low quality SDSS-III/BOSS spectra ($0.75 < S/N \text{ per pixel} < 3$)¹ or with bad spectra are re-observed.

Finally, quasars within $1''$ of a radio detection in the FIRST point source catalog (Becker et al. 1995) are targeted.

A fully detailed description of the quasar target selection in SDSS-IV/eBOSS and a discussion of its performance can be found in Myers et al. (2015).

TDSS targets point sources that are selected to be variable in the g , r and i bands using the SDSS-DR9 imaging data (Ahn et al. 2012) and the multi-epoch Pan-STARRS1 (PS1) photometry (Kaiser et al. 2002, 2010). The survey does not specifically target quasars in general but a significant fraction of targets belong to this class (Morganson et al. 2015). Furthermore, there are smaller sub-programs (comprising 10% of the main TDSS survey) that target quasars specifically (MacLeod et al. 2017). Therefore, these quasars are included in the parent sample for the quasar catalog.

Finally, the AGN component of SPIDERS targets X-ray sources detected in the concatenation of the Bright and Faint ROSAT All Sky Survey (RASS) catalogs (Voges et al. 1999, 2000) and that have an optical counterpart detected in the DR9 imaging data (Ahn et al. 2012). Objects with $17 < r < 22$ that lie within $1'$ of a RASS source are targeted. Details about the AGN target selection are available in Dwelly et al. (2017).

2.3. Spectroscopy

Spectroscopic data for SDSS-IV are acquired in a similar manner as for SDSS-III (Dawson et al. 2016). Targets identified by

¹ This measurement refers to the standard SDSS spectroscopic sampling of 69 km s^{-1} per pixel.

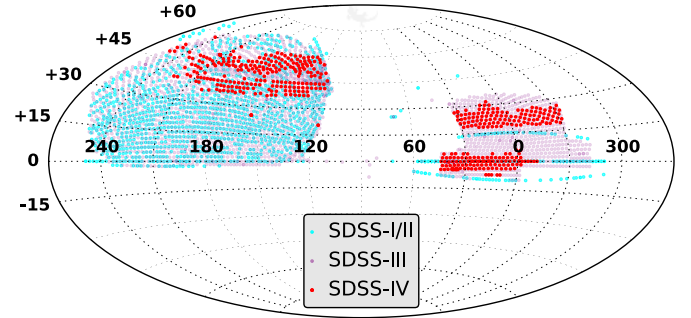


Fig. 1. Distribution on the sky of the SDSS-DR14/eBOSS spectroscopy in J2000 equatorial coordinates (expressed in decimal degrees). Cyan dots correspond to the 1462 plates observed as part of SDSS-I/II. The purple area indicates the 2587 plates observed as part of SDSS-III/BOSS. The red area represents to the 496 new plates observed as part of SDSS-IV (i.e. with MJD $\geq 56\,898$).

the various selection algorithms are observed with the BOSS spectrographs whose resolution varies from ~ 1300 at 3600 \AA to 2500 at $10\,000 \text{ \AA}$ (Smee et al. 2013). Spectroscopic observations are obtained in a series of at least three 15-min exposures. Additional exposures are taken until the squared signal-to-noise ratio $(S/N)^2$ per pixel reaches the survey-quality threshold for each CCD. These thresholds are $(S/N)^2 \geq 22$ at i -band magnitude for the red camera and $(S/N)^2 \geq 10$ at g -band magnitude for the blue camera (Galactic extinction-corrected magnitudes). The spectroscopic reduction pipeline for the BOSS spectra is described in Bolton et al. (2012). SDSS-IV uses plates covered by 1000 fibers that have a field of view of approximately 7 deg^2 . The plates are tiled in a manner which allows them to overlap (Dawson et al. 2016). Figure 1 shows the locations of observed plates. The total area covered by the DR 14 of SDSS-IV/eBOSS is 2044 deg^2 . Figure 2 presents the number of spectroscopically confirmed quasars with respect to their observation date.

3. Construction of the DR14Q catalog

Unlike the SDSS-III/BOSS quasar catalogs (Pâris et al. 2012, 2014, 2017), the SDSS-IV quasar catalog also contains all the quasars observed as part of SDSS-I/II/III. This decision is driven by one of the scientific goals of SDSS-IV/eBOSS to use quasars as the tracers of large scale structures at $z \sim 1.5$ (see Dawson et al. 2016; Blanton et al. 2017): quasars observed as part of the first two iterations of SDSS with a high-quality spectrum, i.e. a spectrum from which one can measure a redshift, were not re-observed as part of SDSS-IV (see Myers et al. 2015, for further details).

3.1. Definition of the superset

The ultimate goal of the SDSS quasar catalog is to gather all the quasars observed as part of any of the stages of SDSS (York et al. 2000; Eisenstein et al. 2011; Blanton et al. 2017). To do so, we need to create a list of quasar targets as complete as possible that we refer to as the *superset*. Its definition for the DR14Q catalog depends on the iteration of the SDSS during which a quasar was observed:

- SDSS-I/II: we use the list of confirmed quasars in the SDSS-DR7 quasar catalog that contains all spectroscopically confirmed quasars from SDSS-I/II (Schneider et al. 2010). A total of 79 487 quasars with no re-observation in SDSS-III/IV are included in the superset for DR14Q;

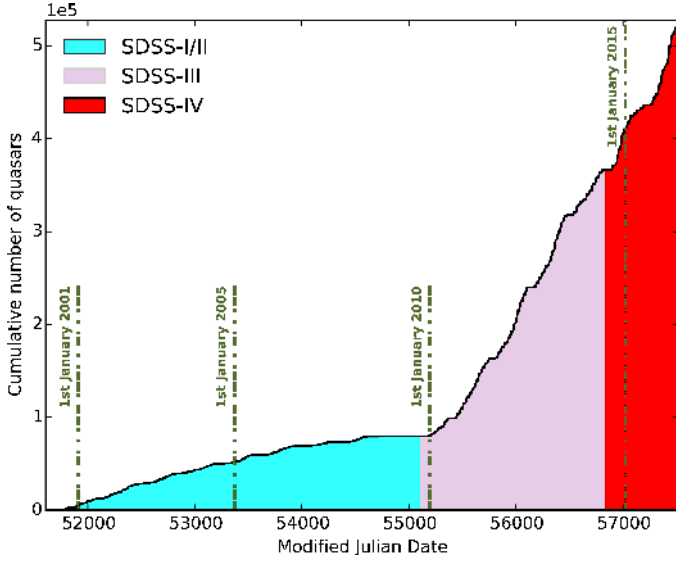


Fig. 2. Cumulative number of quasars as a function of observation date during all the iterations of SDSS (York et al. 2000; Eisenstein et al. 2011; Blanton et al. 2017). Vertical lines show the equivalence between modified Julian dates and usual calendar dates. A total of 526 356 quasars have been spectroscopically confirmed. The “flat portions” in this figure correspond to annual summer shutdown for the telescope maintenance.

- SDSS-III/IV: we follow the definition of the superset as in Pâris et al. (2017). Our input list of quasar targets is composed of all quasar targets as defined by their target selection bits. The full list of programs targeting quasars and associated references is given in Table 1. This set contains objects targeted as part of the legacy programs but also all the ancillary programs that targeted quasars for specific projects (see e.g. Dawson et al. 2013, for examples of ancillary programs). A total of 819 611 quasar targets are identified using target selection bits described in Table 1.

The superset we obtain contains 899 098 objects to be classified.

3.2. Automated classification

Given the increase of the number of quasar targets in SDSS-IV, the systematic visual inspection we performed in SDSS-III/BOSS (e.g. Pâris et al. 2012) is no longer feasible. Since the output of the SDSS pipeline (Bolton et al. 2012) cannot be fully efficient to classify quasar targets, we adopt an alternate strategy: starting from the output of the SDSS pipeline, we identify SDSS-IV quasar targets for which it is likely the identification and redshifts are inaccurate. This set of objects is visually inspected following the procedure described in Sect. 3.3.

The spectra of quasar candidates are reduced by the SDSS pipeline², which provides a classification (QSO, STAR or GALAXY) and a redshift. This task is accomplished using a library of stellar templates and a principal component analysis (PCA) decomposition of galaxy and quasar spectra are fitted to each spectrum. Each class of templates is fitted in a given range of redshift: galaxies from $z = -0.01$ to 1.00, quasars from $z = 0.0033$ to 7.00, and stars from $z = -0.004$ to 0.004 ($\pm 1200 \text{ km s}^{-1}$). For each spectrum, the fits are ordered by increasing reduced χ^2 ; the overall best fit is the fit with the lowest reduced χ^2 .

² The software used to reduce SDSS data is called `idlpec2d`. Its DR14 version is `v5_10_0`.

We start with the first five identifications, i.e. identifications corresponding to the five lowest reduced χ^2 , redshifts and ZWARNING. The latter is a quality flag. Whenever it is set to 0, its classification and redshift are considered reliable. We then apply the following algorithm:

1. if the first SDSS pipeline identification is STAR, then the resulting classification is STAR;
2. if the first SDSS pipeline identification is GALAXY with $z_{\text{pipeline}} < 1$, then the resulting classification is GALAXY;
3. if the first SDSS pipeline identification is GALAXY with $z_{\text{pipeline}} \leq 1$ and at least two other SDSS pipeline identifications are GALAXY, then the resulting classification is GALAXY;
4. if the first SDSS pipeline identification is QSO with ZWARNING = 0, then the resulting classification is QSO, except if at least two other SDSS pipeline identifications are STAR. In such a case, the resulting identification is STAR;
5. if the first pipeline identification is QSO with ZWARNING > 0 and at least two alternate SDSS pipeline identifications are STAR, then the resulting identification is STAR.

At this stage, the redshift measurement we consider for automatically classified objects is the redshift estimate of the overall best fit of the SDSS pipeline, except if the automated identification is STAR. In that case, we set the redshift to 0. If an object does not pass any of these conditions, the resulting classification is UNKNOWN and it is added to the list of objects that require visual inspection (see Sect. 3.3).

In order to achieve the expected precision on the $d_A(z)$ and $H(z)$ measurements, it is required (i) to have <1% of actual quasars lost in the classification process and (ii) to have <1% of contaminants in the quasar catalog. We tested this algorithm against the result of the full visual inspection of the “SEQUELS” pilot survey of SDSS-IV/eBOSS that contains a total of 36 489 objects (see Myers et al. 2015; Pâris et al. 2017, for details) to ensure that these requirements are fulfilled.

Out of these 36 489 objects, 2393 (6.6% of the whole sample) cannot be classified by the automated procedure, 18 799 are classified as QSO, 10 001 as STAR, and 5288 as GALAXY. For objects identified as QSO by the algorithm, 98 are wrongly classified. This represents a contamination of the quasar sample of 0.5%. A total of 158 actual quasars, i.e. identified in the course of the full visual inspection, are lost which represents 0.8% of the whole quasar sample. The latter number includes 12 objects identified as QSO_Z? by visual inspection because their identification is not ambiguous. Detailed results for the comparison with the fully visually inspected sample are provided in Table 2.

The performance of this algorithm depends on the SDSS pipeline version and the overall data quality. To ensure that this performance does not change significantly, we fully visually inspect randomly picked plates regularly and test the quality of the output.

3.3. Visual inspection process

Depending on the iteration of SDSS, different visual inspection strategies have been applied.

3.3.1. Systematic visual inspection of SDSS-III quasar candidates

As described in Pâris et al. (2012), we visually inspected all quasar targets observed in SDSS-III/BOSS (Eisenstein et al.

Table 1. Programs from SDSS-III/BOSS (Eisenstein et al. 2011; Dawson et al. 2013) and SDSS-IV (Dawson et al. 2016; Blanton et al. 2017) targeting quasars and taken as inputs to build up the SDSS-DR14 quasar catalog.

Bit	Selection	Bit	Selection	Bit	Selection	Bit	Selection
BOSS_TARGET1							
10	QSO_CORE ⁽¹⁾	11	QSO_BONUS ⁽¹⁾	12	QSO_KNOWN_MIDZ ⁽¹⁾	13	QSO_KNOWN_LOHIZ ⁽¹⁾
14	QSO_NN ⁽¹⁾	15	QSO_UKIDSS ⁽¹⁾	16	QSO_LIKE_COADD ⁽¹⁾	17	QSO_LIKE ⁽¹⁾
18	QSO_FIRST_BOSS ⁽¹⁾	19	QSO_KDE ⁽¹⁾	40	QSO_CORE_MAIN ⁽¹⁾	41	QSO_BONUS_MAIN ⁽¹⁾
42	QSO_CORE_ED ⁽¹⁾	43	QSO_CORE_LIKE ⁽¹⁾	44	QSO_KNOWN_SUPPZ ⁽¹⁾		
ANCILLARY_TARGET1							
6	BLAZGVAR ⁽²⁾	7	BLAZR ⁽²⁾	8	BLAZXR ⁽²⁾	9	BLAZXRSAL ⁽²⁾
10	BLAZXRVAR ⁽²⁾	11	XMMBRIGHT ⁽²⁾	12	XMMGRIZ ⁽²⁾	13	XMMHR ⁽²⁾
14	XMMRED ⁽²⁾	15	FBQSBAL ⁽²⁾	16	LBQSBAL ⁽²⁾	17	ODDBAL ⁽²⁾
18	OTBAL ⁽²⁾	19	PREVBAL ⁽²⁾	20	VARBAL ⁽²⁾	22	QSO_AAL ⁽²⁾
23	QSO_AALS ⁽²⁾	24	QSO_IAL ⁽²⁾	25	QSO_RADIO ⁽²⁾	26	QSO_RADIO_AAL ⁽²⁾
27	QSO_RADIO_IAL ⁽²⁾	28	QSO_NOAALS ⁽²⁾	29	QSO_GRI ⁽²⁾	30	QSO_HIZ ⁽²⁾
31	QSO_RIZ ⁽²⁾	50	BLAZGRFLAT ⁽²⁾	51	BLAZGRQSO ⁽²⁾	52	BLAZGX ⁽²⁾
53	BLAZGXQSO ⁽²⁾	54	BLAZGXR ⁽²⁾	55	BLAZXR ⁽²⁾	58	CXOBRIGHT ⁽²⁾
59	CXORED ⁽²⁾						
ANCILLARY_TARGET2							
0	HIZQSO82 ⁽²⁾	1	HIZQSOIR ⁽²⁾	2	KQSO_BOSS ⁽²⁾	3	QSO_VAR ⁽²⁾
4	QSO_VAR_FPG ⁽²⁾	5	RADIO_2LOBE_QSO ⁽²⁾	7	QSO_SUPPZ ⁽²⁾	8	QSO_VAR_SDSS ⁽²⁾
9	QSO_WISE_SUPP ⁽³⁾	10	QSO_WISE_FULL_SKY ⁽⁴⁾	13	DISKEMITTER_REPEAT ⁽⁴⁾	14	WISE_BOSS_QSO ⁽⁴⁾
15	QSO_XD_KDE_PAIR ⁽⁴⁾	24	TDSS_PILOT ⁽⁴⁾	25	SPIDERS_PILOT ⁽⁴⁾	26	TDSS_SPIDERS_PILOT ⁽⁴⁾
27	QSO_VAR_LF ⁽⁴⁾	31	QSO_EBOSS_W3_ADM ⁽⁴⁾	32	XMM_PRIME ⁽⁴⁾	33	XMM_SECOND ⁽⁴⁾
53	SEQUELS_TARGET ⁽⁴⁾	54	RM_TILE1 ⁽⁴⁾	55	RM_TILE2 ⁽⁴⁾	56	QSO_DEEP ⁽⁴⁾
EBOSS_TARGET0							
10	QSO_EBOSS_CORE ⁽⁵⁾	11	QSO_PTF ⁽⁵⁾	12	QSO_REOBS ⁽⁵⁾	13	QSO_EBOSS_KDE ⁽⁵⁾
14	QSO_EBOSS_FIRST ⁽⁵⁾	15	QSO_BAD_BOSS ⁽⁵⁾	16	QSO_BOSS_TARGET ⁽⁵⁾	17	QSO_SDSS_TARGET ⁽⁵⁾
18	QSO_KNOWN ⁽⁵⁾	20	SPIDERS_RASS_AGN ⁽⁶⁾	22	SPIDERS_ERASS_AGN ⁽⁶⁾	30	TDSS_A ⁽⁷⁾
31	TDSS_FES_DE ⁽⁸⁾	33	TDSS_FES_NQHISN ⁽⁸⁾	34	TDSS_FES_MGII ⁽⁸⁾	35	TDSS_FES_VARBAL ⁽⁸⁾
40	SEQUELS_PTF_VARIABLE						
EBOSS_TARGET1							
9	QSO1_VAR_S82 ⁽⁹⁾	10	QSO1_EBOSS_CORE ⁽⁵⁾	11	QSO1_PTF ⁽⁵⁾	12	QSO1_REOBS ⁽⁵⁾
13	QSO1_EBOSS_KDE ⁽⁵⁾	14	QSO1_EBOSS_FIRST ⁽⁵⁾	15	QSO1_BAD_BOSS ⁽⁵⁾	16	QSO_BOSS_TARGET ⁽⁵⁾
17	QSO_SDSS_TARGET ⁽⁵⁾	18	QSO_KNOWN ⁽⁵⁾	30	TDSS_TARGET ^(7,8,10)	31	SPIDERS_TARGET ^(6,10)
EBOSS_TARGET2							
0	SPIDERS_RASS_AGN ⁽⁶⁾	2	SPIDERS_ERASS_ANG ⁽⁶⁾	4	SPIDERS_XMMSL_AGN ⁽⁶⁾	20	TDSS_A ⁽⁷⁾
21	TDSS_FES_DE ⁽⁸⁾	23	TDSS_FES_NQHISN ⁽⁸⁾	24	TDSS_FES_MGII ⁽⁸⁾	25	TDSS_FES_VARBAL ⁽⁸⁾
26	TDSS_B ⁽⁷⁾	27	TDSS_FES_HYPQSO ⁽⁸⁾	31	TDSS_CP ⁽⁸⁾	32	S82X_TILE1 ⁽¹⁰⁾
33	S82X_TILE2 ⁽¹⁰⁾	34	S82X_TILE3 ⁽¹⁰⁾	50	S82X_BRIGHT_TARGET ⁽¹⁰⁾	51	S82X_XMM_TARGET ⁽¹⁰⁾
52	S82X_WISE_TARGET ⁽¹⁰⁾			53	S82X_SACLAY_VAR_TARGET ⁽¹⁰⁾		
54	S82X_SACLAY_BDT_TARGET ⁽¹⁰⁾			55	S82X_SACLAY_HIZ_TARGET ⁽¹⁰⁾		
56	S82X_RICHARDS15_PHOTOQSO_TARGET ⁽¹⁰⁾			57	S82X_PETERS15_COLORVAR_TARGET ⁽¹⁰⁾		
58	S82X_LSSTZ4_TARGET ⁽¹⁰⁾			59	S82X_UNWISE_TARGET ⁽¹⁰⁾		
60	S82X_GTRADMZ4_TARGET ⁽¹⁰⁾			61	S82X_CLAGN1_TARGET ⁽¹⁰⁾		
62	S82X_CLAGN2_TARGET ⁽¹⁰⁾						

References. ⁽¹⁾ Ross et al. (2012). ⁽²⁾ Dawson et al. (2013). ⁽³⁾ Ahn et al. (2014). ⁽⁴⁾ Alam et al. (2015). ⁽⁵⁾ Myers et al. (2015). ⁽⁶⁾ Dwelly et al. (2017). ⁽⁷⁾ Morganson et al. (2015). ⁽⁸⁾ MacLeod et al. (2017). ⁽⁹⁾ Palanque-Delabrouille et al. (2016). ⁽¹⁰⁾ Abolfathi et al. (2017).

2011; Dawson et al. 2013). The idea was to construct a quasar catalog as complete and pure as possible (this was also the approach adopted by SDSS-I/II catalogs). Several checks during the SDSS-III/BOSS survey have shown that completeness (within the given target selection) and purity are larger than 99.5%.

After their observation, all the spectra are automatically classified by the SDSS pipeline (Bolton et al. 2012). Spectra are divided into four categories based on their initial classification by the SDSS pipeline: low-redshift quasars (i.e. $z < 2$), high-redshift quasars (i.e. $z \geq 2$), stars and others. We perform the

visual inspection plate by plate through a dedicated website: all spectra for a given category can be validated at once if their identification and redshift are correct. If an object requires further inspection or a change in its redshift, we have the option to go to a detailed page on which not only the identification can be changed but also BALs and DLAs can be flagged and the redshift can be adjusted. When possible the peak of the Mg II emission line was used as an estimator of the redshift (see Pâris et al. 2012), otherwise the peak of C IV was taken as the indicator in case the redshift given by the pipeline was obviously in error.

Table 2. Comparison between the automated classification scheme based on the output of the SDSS pipeline (Bolton et al. 2012) and visual inspection of our training set.

Visual inspection	Automated classification			
	UNKNOWN	QSO	STAR	GALAXY
QSO	1418	17 687	27	107
QSO_BAL	144	946	4	8
QSO_?	79	27	6	26
QSO_Z?	120	41	5	7
Star	213	11	9804	189
Star_?	61	5	54	29
Galaxy	74	37	23	4623
?	115	15	34	95
Bad	169	30	44	204

3.3.2. Residual visual inspection of SDSS-IV quasar candidates

For SDSS-IV/eBOSS, we visually inspect only the objects the automated procedure considers ill-identified. Most of the corresponding spectra are, unsurprisingly, of low S/N. A number of ill-identified sources have good S/N but show strong absorption lines which confuse the pipeline. These objects can be strong BALs but also spectra with a strong DLA at the emission redshift (Finley et al. 2013; Fathivavari et al. 2017). A few objects have very unusual continua. The visual inspection itself proceeds as for the SDSS-III/eBOSS survey. However, we no longer visually flag BALs and we change redshifts only in case of catastrophic failures of the SDSS pipeline.

3.4. Classification result

Starting from the 899 098 unique objects included in the DR14Q superset, we run the automated procedure described in Sect. 3.2. A total of 42 729 quasar candidates are classified as UNKNOWN by the algorithm. Identification from the full visual inspection of SDSS-I/II/III quasar targets was already available for 625 432 objects, including 32 621 identified as UNKNOWN by the automated procedure. The remaining 10 108 quasar candidates with no previous identification from SDSS-I/II/III have been visually inspected. After merging all the already existing identifications, 635 540 objects are identified through visual inspection and 263 558 are identified by the automated procedure.

A total of 526 356 quasars are identified, 387 223 from visual inspection and 139 133 from the automated classification. Results are summarized in Table 3.

4. Redshift estimate

Despite the presence of large and prominent emission lines, it is frequently difficult to estimate accurate redshifts for quasars. Indeed, the existence of quasar outflows create systematic shifts in the location of broad emission lines leading to not fully controlled errors in the measurement of redshifts (e.g. Shen et al. 2016). Accuracy in this measurement is crucial to achieve the scientific goals of SDSS-IV/eBOSS. As stated in the Sect. 5.2 of Dawson et al. (2016), we mitigate this problem by using two different types of redshift estimates: one based on the result of a principal component analysis and another one based on the location of the maximum of the peak of the Mg II emission line.

4.1. Automated redshift estimates

Various studies have shown that the Mg II emission line is the quasar broad emission line that is the least affected by systematic shifts (e.g. Hewett & Wild 2010; Shen et al. 2016). In the BOSS spectral range, this feature is available in the redshift range 0.3–2.5, which covers most of our sample.

To measure the Mg II redshift (Z_{MGII}), we first perform a principal component analysis (PCA) on a sample of 8986 SDSS-DR7 quasars (Schneider et al. 2010) using input redshifts from Hewett & Wild (2010). The detailed selection of this sample is explained in Sect. 4 of Pâris et al. (2012). With the resulting set of eigenspectra, we fit a linear combination of five principal components and measure the location of the maximum of the Mg II emission line. This first step produces a new redshift measurement that can be used to re-calibrate our reference sample. We then perform another PCA with Z_{MGII} and derive a new set of principal components. In this second step it is not necessary to have Z_{MGII} but this step is mandatory to derive PCA redshifts calibrated to use the Mg II emission as a reference.

Finally, to measure Z_{PCA} , we fit a linear combination of four eigenspectra to all DR14Q spectra. The redshift estimate is an additional free parameter in the fit. During the fitting process, there is an iterative removal of absorption lines in order to limit their impact on redshift measurements; Details are given in Pâris et al. (2012).

4.2. Comparison of redshift estimates provided in DR14Q

In the present catalog, we release four redshift estimates: Z_{PIPE} , Z_{VI} , Z_{PCA} , and Z_{MGII} . As explained in the previous section, the Mg II emission line is the least affected broad emission line in quasar spectra. In addition, this emission line is available for most of our sample. We use it as the reference redshift to test the accuracy of our three other redshift estimates. For this test, we select all the DR14Q quasars for which we have the four redshift estimates. Among these 178 981 objects, we also select 151 701 CORE quasars only to test the behavior of our estimates on this sample for which redshift accuracy is crucial. Figure 3 displays the distribution of the velocity differences between Z_{VI} , Z_{PIPE} , Z_{PCA} and Z_{MGII} for the full sample having the four redshift estimates available (left panel) and CORE quasars only (right panel). Table 4 gives the systematic shift for each of the distributions and the dispersion of these quantities, expressed in km s^{-1} , for both samples.

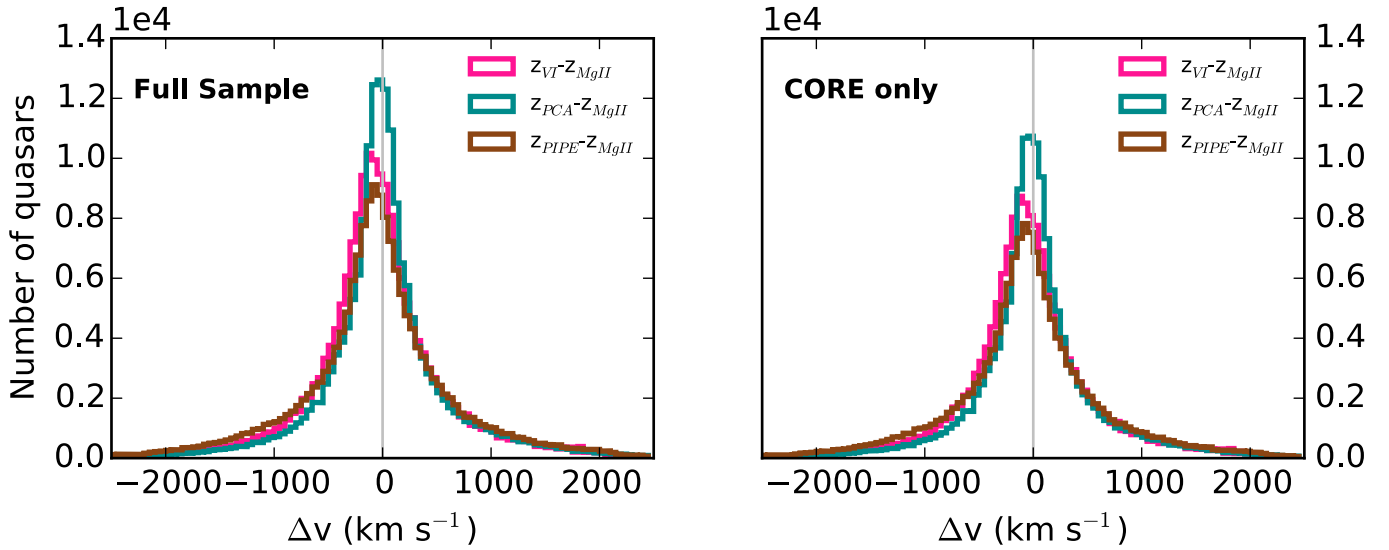
As explained in Sect. 3.3, the visual inspection redshift Z_{VI} is set to be at the location of the maximum of the Mg II emission line when this line is available. With this strategy, the systematic shift with respect to the Mg II emission line is limited by the accuracy of the visual inspection. Although it is a time-consuming approach, this redshift estimate produces an extremely low number of redshift failures (<0.5%), leading to a low dispersion around this systematic shift.

The SDSS pipeline redshift estimate, Z_{PIPE} , is the result of a principal component analysis performed on a sample of visually-inspected quasars. Hence, Z_{PIPE} is expected to have a similar systematic shift as Z_{VI} . On the other hand, Z_{PIPE} is subject to more redshift failures due to peculiar objects or low S/N spectra and thus the larger dispersion of the velocity difference distribution seen in Fig. 3 and Table 4.

Z_{PCA} is also the result of a principal component analysis but, unlike Z_{PIPE} , the reference sample has been carefully chosen to have an automated redshift corresponding to the location

Table 3. Result of our classification process, split between automated and visual inspection classifications.

Number of quasar targets in SDSS-III/IV	819 611
Number of quasars from SDSS-I/II only	79 487
Total number of objects in DR14Q superset	899 098
Number of targets with automated classification	263 558
Number of targets with visual inspection classification	635 540
Number of quasars from automated classification	139 133
Number of quasars from visual inspection classification	387 223
Total number of DR14Q quasars	526 356


Fig. 3. *Left panel:* distribution of velocity differences between Z_{VI} (magenta histogram), Z_{PIPE} (brown histogram), Z_{PCA} (dark cyan histogram) and Z_{MgII} . These histograms are computed using 178 981 quasars that have all the four redshift estimates available in DR14Q. *Right panel:* same as left panel restricted to the 151 701 CORE quasars for which we have the four redshift estimates available in DR14Q. In *both panels*, the histograms are computed in bins of $\Delta v = 50 \text{ km s}^{-1}$ and the vertical grey line marks $\Delta v = 0 \text{ km s}^{-1}$.

of the maximum of the Mg II emission line. Therefore, a systematic shift smaller than 10 km s^{-1} was expected when compared to Z_{MgII} . In addition, Z_{PCA} takes into account the possible presence of absorption lines, even broad ones, and it is trained to ignore them. Z_{PCA} is thus less sensitive to peculiarities in quasar spectra, which explains the reduced dispersion of redshift errors when compared to Z_{PIPE} .

A similar analysis performed on a sample of 151 701 CORE quasars for which we have the four redshift estimates leads to similar results for redshift estimates. These exercises demonstrate that there is no additional and significant systematics for the redshift estimate of the CORE quasar sample.

5. Broad absorption line quasars

In SDSS-III/BOSS, we performed a full visual inspection of all quasar targets. During this process, we visually flagged spectra displaying BALs. With this catalog, it is no longer possible to visually inspect all BALs and we now rely on a fully automated detection of BALs.

As for the previous SDSS quasar catalogs, we automatically search for BAL features and report metrics of common use in the community: the BALnicity Index (BI; Weymann et al. 1991) of the C IV absorption troughs. We restrict the automatic search to quasars with $z \geq 1.57$ in order to have the full spectral coverage of C IV absorption troughs. The BALnicity Index (Col. #32) is

Table 4. Median shift and dispersion of velocity differences between Z_{VI} , Z_{PIPE} , Z_{PCA} and Z_{MgII} for the full DR14Q sample and the CORE sample only.

	Median Δv (km s^{-1})	$\sigma_{\Delta v}$ (km s^{-1})
Full sample (178 981 quasars)		
$Z_{VI} - Z_{MgII}$	-59.7	585.9
$Z_{PIPE} - Z_{MgII}$	-54.8	697.2
$Z_{PCA} - Z_{MgII}$	-8.8	586.9
CORE sample (151 701 quasars)		
$Z_{VI} - Z_{MgII}$	-61.7	581.0
$Z_{PIPE} - Z_{MgII}$	-57.9	692.1
$Z_{PCA} - Z_{MgII}$	-9.3	577.4

Notes. These numbers are derived from a subsample of 178 981 quasars from DR14Q for which we have the four redshift estimates available. We also restrict this analysis to 151 701 CORE quasars for which we also have the four different redshift estimates. See Fig. 3 for the full distributions.

computed bluewards of the C IV emission line and is defined as:

$$BI = - \int_{25\,000}^{3000} \left[1 - \frac{f(v)}{0.9} \right] C(v) dv, \quad (1)$$

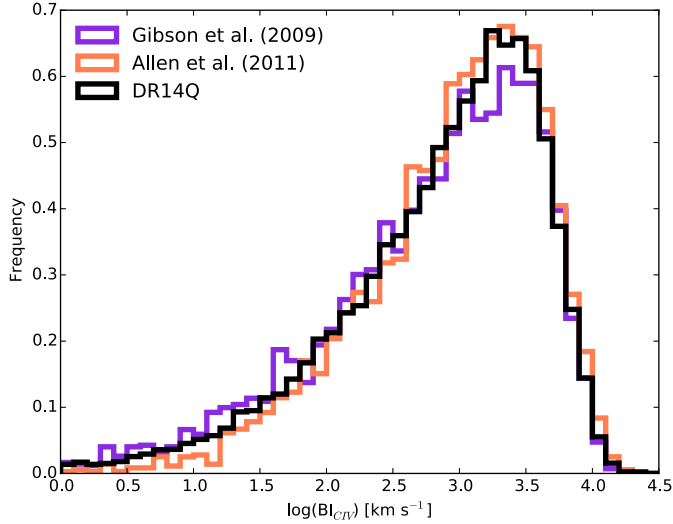


Fig. 4. Distribution of the logarithm of the CIV BALnicity Index for BAL quasars in DR14Q (black histogram), (Gibson et al. 2009, violet histogram) and (Allen et al. 2011, orange histogram). All the histograms are normalized to have their sum equal to one. Histograms have bin widths of $\log \text{BI}_{\text{CIV}} = 0.1$.

where $f(v)$ is the normalized flux density as a function of velocity displacement from the emission-line center. The quasar continuum is estimated using the linear combination of four principal components as described in Sect. 4.1. $C(v)$ is initially set to 0 and can take only two values, 1 or 0. It is set to 1 whenever the quantity $1 - f(v)/0.9$ is continuously positive over an interval of at least 2000 km s^{-1} . It is reset to 0 whenever this quantity becomes negative. CIV absorption troughs wider than 2000 km s^{-1} are detected in the spectra of 21 877 quasars.

The distribution of BI for CIV troughs from DR14Q is presented in Fig. 4 (black histogram) and is compared to previous works by Gibson et al. (2009, purple histogram) performed on DR5Q (Schneider et al. 2007) and by Allen et al. (2011, orange histogram) who searched for BAL quasars in quasar spectra released as part of SDSS-DR6 (Adelman-McCarthy et al. 2008). The three distributions are normalized to have their sum equal to one. The overall shapes of the three distributions are similar. The BI distribution from Gibson et al. (2009) exhibits a slight excess of low-BI values ($\log \text{BI}_{\text{CIV}} < 2$) compared to Allen et al. (2011) and this work. The most likely explanation is the difference in the quasar emission modeling. Allen et al. (2011) used a non-negative matrix factorization (NMF) to estimate the unabsorbed flux, which produces a quasar emission line shape akin to the one we obtain with PCA. Gibson et al. (2009) modeled their quasar continuum with a reddened power-law and strong emission lines with Voigt profiles. Power-law like continua tend to underestimate the actual quasar emission and hence, the resulting BI values tend to be lower than the one computed when the quasar emission is modeled with NMF or PCA methods.

6. Summary of the sample

The DR14Q catalog contains 526 356 unique quasars, of which 144 046 are new discoveries since the previous release. This dataset represents an increase of about 40% in the number of SDSS quasars since the beginning of SDSS-IV. Spectroscopic observations of quasars were performed over 9376 deg^2 for SDSS-I/II/III. New SDSS-IV spectroscopic data are available over 2044 deg^2 . The average surface density of $0.9 < z < 2.2$

quasars prior to the beginning of SDSS-IV is 13.27 deg^{-2} , and reaches 80.24 deg^{-2} in regions for which SDSS-IV spectroscopy is available. The overall quasar surface density in regions with SDSS-IV spectroscopy is 125.03 deg^{-2} , which corresponds to an increase by a factor of 2.4 times compared to the previous quasar catalog release.

The redshift distribution of the full sample is shown in Fig. 5 (left panel; black histogram). Redshift distributions of quasars observed by each phase of SDSS are also presented in the left panel of Fig. 5: SDSS-I/II in cyan, SDSS-III in purple and SDSS-IV in red. SDSS-I/II has observed quasars in the redshift range 0–5.4 with an almost flat distribution up to $z \sim 2.5$, and then a steep decrease. SDSS-III has focused on $z \geq 2.15$ quasars in order to access the Lyman- α forest. The two peaks at $z \sim 0.8$ and $z \sim 1.6$ are due to known degeneracies in the associated quasar target selection (see Ross et al. 2012, for more details). SDSS-IV/eBOSS mostly aims to fill in the gap between $z \sim 0.8$ and $z \sim 2$. It should be noted that some quasars have been observed multiple times throughout the 16 yr of the survey, thus the cumulative number in each redshift bin is larger than the number of objects in each redshift bin for the full sample. The right panel of Fig. 5 shows the redshift distributions for each of the sub-programs using different target selection criteria (Myers et al. 2015). The thick blue histogram indicates the redshift distribution of the CORE sample taking into account previous spectroscopic observations from SDSS-I/II/III. The light blue histogram is the redshift distribution of new SDSS-IV CORE quasars, i.e. those that have been observed later than July 2014. The thick brown histogram displays the redshift distribution of all the variability-selected quasars, i.e. including quasars that were spectroscopically confirmed in SDSS-I/II/III. The orange histogram represents the redshift distribution of newly confirmed variability-selected quasars by SDSS-IV. The green histogram represents the redshift distribution of quasars that were targeted for recent spectra as TDSS variables (Morganson et al. 2015; MacLeod et al. 2017). Further discussion of the redshift distribution of TDSS-selected quasars can be found in Ruan et al. (2016). All the quasars selected by other programs, such as ancillary programs in SDSS-III or special plates, have their redshift distribution indicated in pink.

A similar comparison is done for the Galactic-extinction corrected r -band magnitudes of DR14Q quasars in Fig. 6 using the same color code as in Fig. 5. The left panel of Fig. 6 shows the r -band magnitude (corrected for Galactic extinction) distributions of quasars observed by each iteration of SDSS. The right panel of Fig. 6 displays the r -band magnitude distribution for each of the subsamples (CORE, variability-selected quasars, TDSS and ancillary programs).

Finally, we present a density map of the DR14Q quasars in the $L - z$ plane in Fig. 7. The area covered in this plane by each phase of SDSS is also displayed. SDSS-I/II (cyan contour) has observed the brightest quasars at all redshifts. SDSS-III (purple contour) has observed up to two magnitudes deeper than SDSS-I/II, mostly at $z > 2$. SDSS-IV (red contour) is observing at the same depth as for SDSS-III but at lower redshift, i.e. focusing on the redshift range 0.8–2.2.

7. Multi-wavelength cross-correlation

We provide multi-wavelength matching of DR14Q quasars to several surveys: the FIRST radio survey (Becker et al. 1995), the Galaxy Evolution Explorer (GALEX, Martin et al. 2005) survey in the UV, the Two Micron All Sky Survey (2MASS,

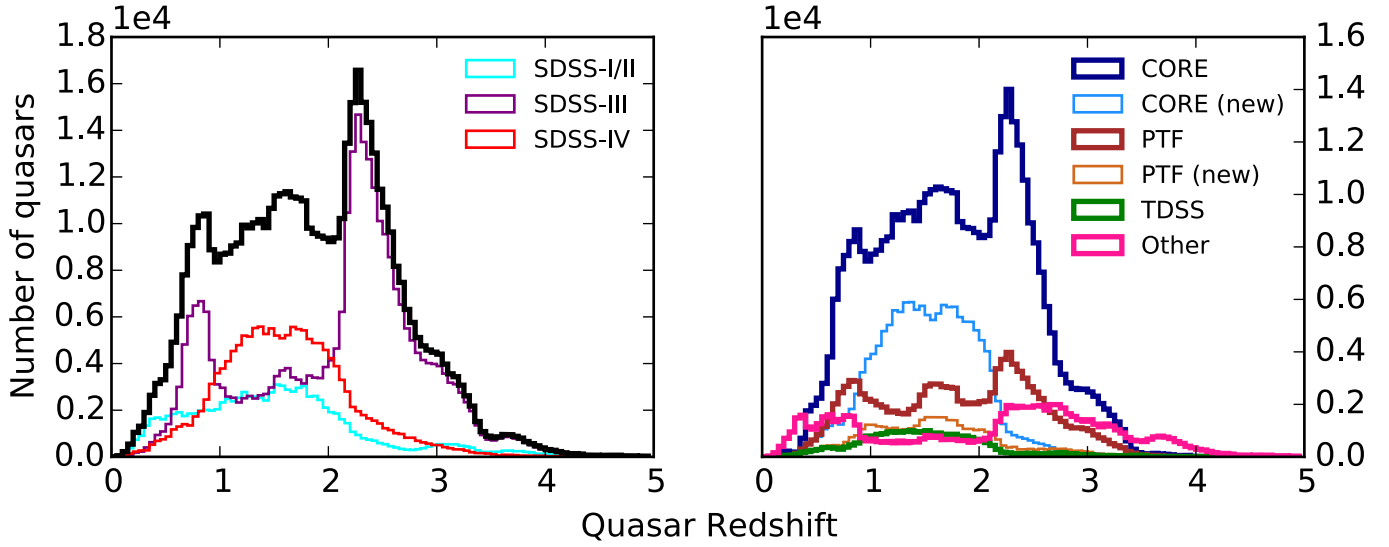


Fig. 5. *Left panel:* redshift distribution of DR14Q quasars (black thick histogram) in the range $0 \leq z \leq 5$. The redshift distribution of quasars observed as part of SDSS-I/II is shown with a cyan histogram. The redshift distributions of quasars observed as part of SDSS-III (purple histogram) and SDSS-IV (red histogram) are also displayed. *Right panel:* redshift distributions of all CORE quasars that are part of DR14Q (dark blue histogram), CORE quasars observed as part of SDSS-IV/eBOSS (light blue histogram), all PTF quasars (brown histogram), PTF quasars observed as part of SDSS-IV/eBOSS (orange histogram), SDSS-IV/TDSS quasars (green histogram) and quasars observed as part of ancillary programs (pink histogram). Some quasars can be selected by several target selection algorithms, hence the cumulative number of quasars in a single redshift bin can exceed the total number in that bin. The bin size for *both panels* is $\Delta z = 0.05$.

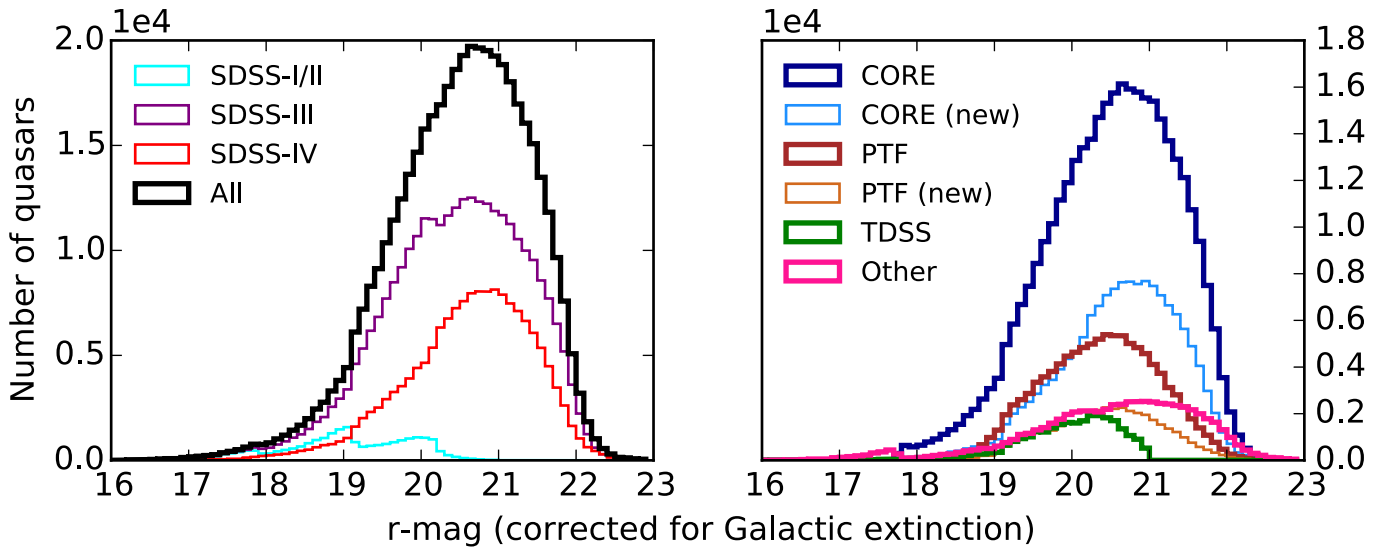


Fig. 6. *Left panel:* distribution of r -band magnitude corrected for Galactic extinction using the [Schlafly & Finkbeiner \(2011\)](#) dust maps for all DR14Q quasars (thick black histogram), quasars observed during SDSS-I/II (cyan histogram), SDSS-III (purple histogram) and SDSS-IV (red histogram). *Right panel:* distribution of r -band magnitude corrected for Galactic extinction for all CORE quasars (dark blue histogram), CORE quasars observed as part of SDSS-IV only (light blue histogram), all PTF quasars (brown histogram), PTF quasars observed as part of SDSS-IV only (orange histogram), SDSS-IV/TDSS quasars (green histogram), and quasars selected as part of ancillary programs (pink histogram). A given quasar can be selected by several target selection algorithms, hence the cumulative number of quasars in a r -band magnitude bin can exceed the total number of objects in it. The bin size for *both panels* is $\Delta r = 0.1$.

(Cutri et al. 2003; Skrutskie et al. 2006), the UKIRT Infrared Deep Sky Survey (UKIDSS; Lawrence et al. 2007), the WISE (Wright et al. 2010), the ROSAT All-Sky Survey (RASS; Voges et al. 1999, 2000), and the seventh data release of the Third *XMM-Newton* Serendipitous Source Catalog (Rosen et al. 2016).

7.1. FIRST

As for the previous SDSS-III/BOSS quasar catalogs, we matched the DR14Q quasars to the latest FIRST catalog (December 2014;

Becker et al. 1995) using a $2''$ matching radius. We report the flux peak density at 20 cm and the S/N of the detection. Among the DR14Q quasars, 73 126 lie outside of the FIRST footprint and have their FIRST_MATCHED flag set to -1 .

A total of 18 273 quasars have FIRST counterparts in DR14Q. We estimate the fraction of chance superpositions by offsetting the declination of DR14Q quasars by $200''$. We then re-match to the FIRST source catalog. We conclude that there are about 0.2% of false positives in the DR14Q-FIRST matching.

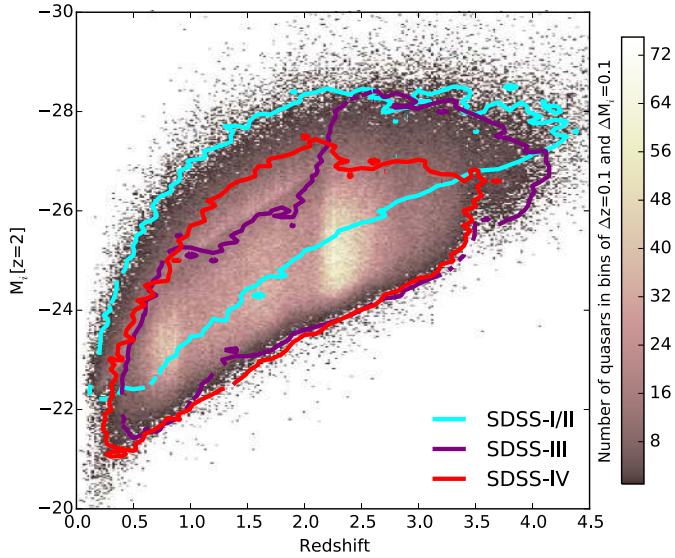


Fig. 7. Density map of the DR14Q quasars in the $L-z$ plane. The color map indicates the number of DR14Q quasars in bins of $\Delta z = 0.1$ and $\Delta M_L [z = 2] = 0.1$. Colored contours correspond to the envelope in the $L-z$ plane for each iteration of SDSS. The absolute magnitudes assume $H_0 = 70 \text{ km s}^{-1} \text{ Mpc}^{-1}$ and the K-correction is given by Richards et al. (2006), who define $K(z = 2) = 0$.

7.2. GALEX

As for DR12Q, GALEX (Martin et al. 2005) images are force-photometered (from GALEX DR 5) at the SDSS-DR8 centroids (Aihara et al. 2011), such that low S/N PSF fluxes of objects not detected by GALEX are recovered, for both the FUV (1350–1750 Å) and NUV (1750–2750 Å) bands when available. A total of 382 838 quasars are detected in the NUV band, 304 705 in the FUV band and 515 728 have non-zero fluxes in both bands.

7.3. 2MASS

We cross-correlate DR14Q with the All-Sky data release Point Source catalog (Skrutskie et al. 2006) using a matching radius of $2''$. We report the Vega-based magnitudes in the J , H and K -bands and their error together with the S/N of the detections. We also provide the value of the 2MASS flag rd_flg[1], which defines the peculiar values of the magnitude and its error for each band³.

There are 16 427 matches in the catalog. This number is quite small compared with the number of DR14Q quasars because the sensitivity of 2MASS is much less than that of SDSS. Applying the same method as described in Sect. 7.1, we estimate that 0.8% of the matches are false positives.

7.4. WISE

We matched the DR14Q to the AllWISE Source Catalog⁴ (Wright et al. 2010; Mainzer et al. 2011). Our procedure is the same as in DR12Q, with a matching radius of $2.0''$. There are 401 980 matches from the AllWISE Source Catalog. Following the procedure described in Sect. 7.1, we estimate the rate of false positive matches to be about 2%, which is consistent with the findings of Krawczyk et al. (2013).

³ see <http://www.ipac.caltech.edu/2mass/releases/allsky/doc/explsup.html> for more details.

⁴ <http://wise2.ipac.caltech.edu/docs/release/allwise/>

We report the magnitudes, their associated errors, the S/N of the detection and reduced χ^2 of the profile-fitting in the four WISE bands centered at wavelengths of 3.4, 4.6, 12 and $22 \mu\text{m}$. These magnitudes are in the Vega system, and are measured with profile-fitting photometry. We also report the WISE catalog contamination and confusion flag, cc_flags, and their photometric quality flag, ph_qual. As suggested on the WISE “Cautionary Notes” page⁵, we recommend using only those matches with cc_flags = “0000” to exclude objects that are flagged as spurious detections of image artifacts in any band. Full details about quantities provided in the AllWISE Source Catalog can be found on their online documentation⁶.

7.5. UKIDSS

As for DR12Q, near infrared images from the UKIRT Infrared Deep Sky Survey (UKIDSS; Lawrence et al. 2007) are force-photometered.

We provide the fluxes and their associated errors, expressed in $\text{W m}^{-2} \text{ Hz}^{-1}$, in the Y , J , H and K bands. The conversion to the Vega magnitudes, as used in 2MASS, is given by the formula:

$$\text{mag}_X = -2.5 \times \log \frac{f_X}{f_{0,X} \times 10^{-26}}, \quad (2)$$

where X denotes the filter and the zero-point values $f_{0,X}$ are 2026, 1530, 1019 and 631 for the Y , J , H and K bands respectively.

A total of 112 012 quasars are detected in at least one of the four bands Y , J , H or K . 111 083 objects are detected in the Y band, 110 691 in the J band, 110 630 in H band, 111 245 in the K band and 108 392 objects have non-zero fluxes in the four bands. Objects with zero fluxes lie outside the UKIDSS footprint. The UKIDSS limiting magnitude is $K \sim 18$ (for the Large Area Survey) while the 2MASS limiting magnitude in the same band is ~ 15.3 . This difference in depth between the two surveys explains the large difference in the numbers of matches with DR14Q.

7.6. ROSAT

As was done for the previous SDSS-III/BOSS quasar catalogs, we matched the DR14Q quasars to the ROSAT all sky survey Faint (Voges et al. 2000) and Bright (Voges et al. 1999) source catalogs with a matching radius of $30''$. Only the most reliable detections are included in our catalog: when the quality detection is flagged as potentially problematic, we do not include the match. A total of 8655 quasars are detected in one of the RASS catalogs. As for the cross-correlations described above, we estimate that 2.1% of the RASS-DR14Q matches are due to chance superposition.

7.7. XMM-Newton

DR14Q was cross-correlated with the seventh data release of the Third XMM-Newton Serendipitous Source Catalog (Rosen et al. 2016)⁷ (3XMM-DR7) using a standard $5.0''$ matching radius. For each of the 14 736 DR14Q quasars with XMM-Newton counterparts, we report the soft (0.2–2 keV), hard (4.5–12 keV)

⁵ http://wise2.ipac.caltech.edu/docs/release/allsky/expsup/sec1_4b.html#unreliab

⁶ http://wise2.ipac.caltech.edu/docs/release/allsky/expsup/sec2_2a.html

⁷ <http://xmmssc.irap.omp.eu/Catalogue/3XMM-DR7/3XMM-DR7.html>

and total (0.2–12 keV) fluxes, and associated errors, that were computed as the weighted average of all the detections in the three *XMM-Newton* cameras (MOS1, MOS2, PN). Corresponding observed X-ray luminosities are computed in each band and are not absorption corrected. All fluxes and errors are expressed in $\text{erg cm}^{-2} \text{s}^{-1}$ and luminosities are computed using the redshift value Z from the present catalog.

8. Description of the DR14Q catalog

The DR14Q catalog is publicly available on the SDSS public website⁸ as a binary FITS table file. All the required documentation (format, name, unit for each column) is provided in the FITS header. It is also summarized in Table A.1.

Notes on the catalog columns:

1. The DR14 object designation, given by the format SDSS Jhhmmss.ss+ddmmss.s; only the final 18 characters are listed in the catalog (i.e. the character string “SDSS J” is dropped). The coordinates in the object name follow IAU convention and are truncated, not rounded.

2–3. The J2000 coordinates (Right Ascension and Declination) in decimal degrees. The astrometry is from SDSS-DR14 (Abolfathi et al. 2017).

4. The 64-bit integer that uniquely describes the objects that are listed in the SDSS (photometric and spectroscopic) catalogs (THING_ID).

5–7. Information about the spectroscopic observation (Spectroscopic plate number, Modified Julian Date, and spectroscopic fiber number) used to determine the characteristics of the spectrum. These three numbers are unique for each spectrum, and can be used to retrieve the digital spectra from the public SDSS database. When an object has been observed more than once, we selected the best quality spectrum as defined by the SDSS pipeline (Bolton et al. 2012), i.e. with SPECPRIMARY = 1.

8. DR14Q compiles all spectroscopic observations of quasars, including SDSS-I/II spectra taken with a different spectrograph. For spectra taken with the SDSS spectrographs, i.e. spectra released prior to SDSS-DR8 (Aihara et al. 2011), SPECTRO is set to “SDSS”. For spectra taken with the BOSS spectrographs (Smee et al. 2013), SPECTRO is set to “BOSS”.

9–11. Quasar redshift (Col. #9) and associated error (Col. #10). This redshift estimate is the most robust for quasar cataloging purposes and it is used as a prior for refined redshift measurements. Values reported in Col. #9 are from different sources: the outcome of the automated procedure described in Sect. 3.2, visual inspection or the BOSS pipeline (Bolton et al. 2012). The origin of the redshift value is given in Col. #11 (AUTO, VI and PIPE respectively).

12. Redshift from the visual inspection, Z_VI, when available. All SDSS-I/II/III quasars have been visually inspected. About 7% of SDSS-IV quasars have been through this process (see Sect. 3.2 for more details).

13–15. Redshift (Z_PIPE, Col. #13), associated error (Z_PIPE_ERR, Col. #14) and quality flag (ZWARNING,

Col. #15) from the BOSS pipeline (Bolton et al. 2012). ZWARNING > 0 indicates uncertain results in the redshift-fitting code.

16–17. Automatic redshift estimate (Z_PCA, Col. #16) and associated error (Z_PCA_ERR, Col. #17) using a linear combination of four principal components (see Sect. 4 for details). When the velocity difference between the automatic PCA and visual inspection redshift estimates is larger than 5000 km s^{-1} , this PCA redshift and error are set to -1 .

18. Redshifts measured from the Mg II emission line from a linear combination of five principal components (see Pâris et al. 2012). The line redshift is estimated using the position of the maximum of each emission line, contrary to Z_PCA (Col. #16) which is a global estimate using all the information available in a given spectrum.

19–24. The main target selection information for SDSS-III/BOSS quasars is tracked with the BOSS_TARGET1 flag bits (Col. #19; see Table 2 in Ross et al. 2012, for a full description). SDSS-III ancillary program target selection is tracked with the ANCILLARY_TARGET1 (Col. #20) and ANCILLARY_TARGET2 (Col. #21) flag bits. The bit values and the corresponding program names are listed in Dawson et al. (2013), and Alam et al. (2015). Target selection information for the SDSS-IV pilot survey (SEQUELS; Dawson et al. 2016; Myers et al. 2015) is tracked with the EBOSS_TARGET0 flag bits (Col. #22). Finally, target selection information for SDSS-IV/eBOSS, SDSS-IV/TDSS and SDSS-IV/SPIDERS quasars is tracked with the EBOSS_TARGET1 and EBOSS_TARGET2 flag bits. All the target selection bits, program names and associated references are summarized in Table 1.

25–31. If a quasar in DR14Q was observed more than once by SDSS-I/II/III/IV, the number of additional SDSS-I/II spectra is given by N_SPEC_SDSS (Col. #25), the number of additional SDSS-III/IV spectra by N_SPEC_BOSS (Col. #26), and the total number by N_SPEC (Col. #27). The associated plate (PLATE_DUPLICATE, MJD (MJD_DUPLICATE), fiber (FIBERID_DUPLICATE) numbers, and spectrograph information (SPECTRO_DUPLICATE) are given in Cols. #28, 29, 30 and 31 respectively. If a quasar was observed N times in total, the best spectrum is identified in Cols. #5–7, the corresponding N_SPEC is $N - 1$, and the first $N - 1$ columns of PLATE_DUPLICATE, MJD_DUPLICATE, FIBERID_DUPLICATE, and SPECTRO_DUPLICATE are filled with relevant information. Remaining columns are set to -1 .

32–33. BALnicity Index (BI; Weymann et al. 1991; Col. #32) for C IV troughs, and associated error (Col. #33), expressed in km s^{-1} . See definition in Sect. 5. The BALnicity Index is measured for quasars with $z > 1.57$ only, so that the trough enters into the BOSS wavelength region. In cases with poor fits to the continuum, the BALnicity Index and its error are set to -1 .

34. The SDSS Imaging Run number (RUN_NUMBER) of the photometric observation used in the catalog.

35–38. Additional SDSS processing information: the photometric processing rerun number (RERUN_NUMBER, Col. #35); the camera column (1–6) containing the image of the object (COL_NUMBER, Col. #36), the field number of the run containing the object (FIELD_NUMBER, Col. #37), and the object

⁸ http://www.sdss.org/dr14/algorithms/qso_catalog

identification number (OBJ_ID, Col. #38; see [Stoughton et al. 2002](#), for descriptions of these parameters).

39–40. DR14 PSF fluxes, expressed in nanomaggies⁹, and inverse variances (not corrected for Galactic extinction) in the five SDSS filters.

41–42. DR14 PSF AB magnitudes ([Oke & Gunn 1983](#)) and errors (not corrected for Galactic extinction) in the five SDSS filters. These magnitudes are Asinh magnitudes as defined in [Lupton et al. \(1999\)](#).

43. The absolute magnitude in the *i* band at $z = 2$ calculated using a power-law (frequency) continuum index of -0.5 . The K-correction is computed using Table 4 from [Richards et al. \(2006\)](#). We use the SDSS primary photometry to compute this value.

44. Galactic extinction in the five SDSS bands based on [Schlafly & Finkbeiner \(2011\)](#).

45. The logarithm of the vignetting-corrected count rate (photons s^{-1}) in the broad energy band (0.1–2.4 keV) from the *ROSAT* All-Sky Survey Faint Source Catalog ([Voges et al. 2000](#)) and the *ROSAT* All-Sky Survey Bright Source Catalog ([Voges et al. 1999](#)). The matching radius was set to $30''$ (see Sect. 7.6).

46. The S/N of the *ROSAT* measurement.

47. Angular separation between the SDSS and *ROSAT* All-Sky Survey locations (in arcsec).

48–49. Soft X-ray flux (0.2–2 keV) from *XMM-Newton* matching, expressed in $\text{erg cm}^{-2} \text{s}^{-1}$, and its error. In the case of multiple observations, the values reported here are the weighted average of all the *XMM-Newton* detections in this band.

50–51. Hard X-ray flux (4.5–12 keV) from *XMM-Newton* matching, expressed in $\text{erg cm}^{-2} \text{s}^{-1}$, and its error. In the case of multiple observations, the reported values are the weighted average of all the *XMM-Newton* detections in this band.

52–53. Total X-ray flux (0.2–12 keV) from the three *XMM-Newton* CCDs (MOS1, MOS2 and PN), expressed in $\text{erg cm}^{-2} \text{s}^{-1}$, and its error. In the case of multiple *XMM-Newton* observations, only the longest exposure was used to compute the reported flux.

54. Total X-ray luminosity (0.2–12 keV) derived from the flux computed in Col. #52, expressed in erg s^{-1} . This value is computed using the redshift value reported in Col. #9 and is not absorption corrected.

55. Angular separation between the *XMM-Newton* and SDSS-DR14 locations, expressed in arcsec.

56. If a SDSS-DR14 quasar matches with GALEX photometry, GALEX_MATCHED is set to 1, 0 if no GALEX match.

57–60. UV fluxes and inverse variances from GALEX, aperture-photometered from the original GALEX images in the two bands FUV and NUV. The fluxes are expressed in nanomaggies.

61–62. The *J* magnitude and error from the Two Micron All Sky Survey All-Sky data release Point Source Catalog ([Cutri et al. 2003](#)) using a matching radius of $2.0''$ (see Sect. 7.3). A non-detection by 2MASS is indicated by a “0.000” in these columns. The 2MASS measurements are in Vega, not AB, magnitudes.

63–64. S/N in the *J* band and corresponding 2MASS jr_d flag that gives the meaning of the peculiar values of the magnitude and its error¹⁰.

65–68. Same as 61–64 for the *H*-band.

69–72. Same as 61–64 for the *K*-band.

73. Angular separation between the SDSS-DR14 and 2MASS positions (in arcsec).

74–75. The *w1* magnitude and error from the Wide-field Infrared Survey Explorer (WISE; [Wright et al. 2010](#)) All-WISE data release Point Source Catalog using a matching radius of $2''$.

76–77. S/N and χ^2 in the WISE *w1* band.

78–81. Same as 74–77 for the *w2*-band.

82–85. Same as 74–77 for the *w3*-band.

86–89. Same as 74–77 for the *w4*-band.

90. WISE contamination and confusion flag.

91. WISE photometric quality flag.

92. Angular separation between SDSS-DR14 and WISE positions (in arcsec).

93. If a SDSS-DR14 quasar matches UKIDSS aperture-photometry data, UKIDSS_MATCHED is set to 1, it is set to 0 if UKIDSS match.

94–101. Flux density and error from UKIDSS, aperture-photometered from the original UKIDSS images in the four bands Y (Cols. #94–95), J (Cols. #96–97), H (Cols. #98–99) and K (Cols. #100–101). The fluxes and errors are expressed in $\text{W m}^{-2} \text{Hz}^{-1}$.

102. If there is a source in the FIRST radio catalog (version December 2014) within $2.0''$ of the quasar position, the FIRST_MATCHED flag provided in this column is set to 1, 0 if not. If the quasar lies outside of the FIRST footprint, it is set to -1 .

103. The FIRST peak flux density, expressed in mJy.

104. The S/N of the FIRST source whose flux is given in Col. #103.

105. Angular separation between the SDSS-DR14 and FIRST positions (in arcsec).

⁹ See <http://www.sdss.org/dr14/algorithms/magnitudes/#nmgy>

¹⁰ see <http://www.ipac.caltech.edu/2mass/releases/allsky/doc/explsup.html>

9. Conclusion

We have presented the quasar catalog of the SDSS-IV/eBOSS survey corresponding to DR 14 of SDSS and resulting from the first 2 yr of SDSS-IV observations. The catalog, DR14Q, contains 526 356 quasars, 144 046 of which are new discoveries. We provide robust identification from the application of an automated procedure and partial visual inspection of about 10% of the sample (likely ill-identified targets by the automated procedure). Refined redshift measurements based on the result of a principal component analysis of the spectra are also given. The present catalog contains about 80% more quasars at $z < 2$ than our previous release (Pâris et al. 2017). As part of DR14Q, we also provide a catalog of 21 877 BAL quasars and their properties. Multi-wavelength matching with GALEX, 2MASS, UKIDSS, WISE, FIRST, RASS, and *XMM-Newton* observations is also provided as part of DR14Q.

The next SDSS public release containing new eBOSS data is scheduled for the summer of 2019 and will contain spectroscopic data after 4 yr of observations, which should represent more than 700 000 quasars.

Acknowledgements. IP acknowledges the support of the OCEVU Labex (ANR-11-LABX-0060) and the A*MIDEX project (ANR-11-IDEX-0001-02) funded by the “Investissements d’Avenir” French government program managed by the ANR. The French Participation Group to SDSS-IV was supported by the Agence Nationale de la Recherche under contracts ANR-16-CE31-0021. A. W. acknowledges support from a Leverhulme Trust Early Career Fellowship. A. D. M. and B. W. L. acknowledge support from National Science Foundation grants 1515404 and 1616168. I. P. thanks warmly the Great and Extremely COol team, especially Samuel Boissier, Jean-Claude Bouret, Sylvain de la Torre, Audrey Delsanti, Olivier Groussin, Olivier Perfect Ilbert, Éric Jullo, Vincent Le Brun, and Sébastien Vives, for encouraging creativity and for dealing with its unexpected consequences. This research has made use of data obtained from the 3XMM *XMM-Newton* serendipitous source catalog compiled by the 10 institutes of the *XMM-Newton* Survey Science Centre selected by ESA. Funding for the Sloan Digital Sky Survey IV has been provided by the Alfred P. Sloan Foundation, the U.S. Department of Energy Office of Science, and the Participating Institutions. SDSS-IV acknowledges support and resources from the Center for High-Performance Computing at the University of Utah. The SDSS web site is www.sdss.org. SDSS-IV is managed by the Astrophysical Research Consortium for the Participating Institutions of the SDSS Collaboration including the Brazilian Participation Group, the Carnegie Institution for Science, Carnegie Mellon University, the Chilean Participation Group, the French Participation Group, Harvard-Smithsonian Center for Astrophysics, Instituto de Astrofísica de Canarias, The Johns Hopkins University, Kavli Institute for the Physics and Mathematics of the Universe (IPMU)/University of Tokyo, Lawrence Berkeley National Laboratory, Leibniz Institut für Astrophysik Potsdam (AIP), Max-Planck-Institut für Astronomie (MPIA Heidelberg), Max-Planck-Institut für Astrophysik (MPA Garching), Max-Planck-Institut für Extraterrestrische Physik (MPE), National Astronomical Observatory of China, New Mexico State University, New York University, University of Notre Dame, Observatório Nacional/MCTI, The Ohio State University, Pennsylvania State University, Shanghai Astronomical Observatory, United Kingdom Participation Group, Universidad Nacional Autónoma de México, University of Arizona, University of Colorado Boulder, University of Oxford, University of Portsmouth, University of Utah, University of Virginia, University of Washington, University of Wisconsin, Vanderbilt University, and Yale University.

References

Abolfathi, B., Aguado, D. S., Aguilar, G., et al. 2018, *ApJS*, 235, 42
 Adelman-McCarthy, J. K., Agüeros, M. A., Allam, S. S., et al. 2008, *ApJS*, 175, 297
 Ahn, C. P., Alexandroff, R., Allende Prieto, C., et al. 2012, *ApJS*, 203, 21
 Ahn, C. P., Alexandroff, R., Allende Prieto, C., et al. 2014, *ApJS*, 211, 17
 Aihara, H., Allende Prieto, C., An, D., et al. 2011, *ApJS*, 193, 29
 Alam, S., Albareti, F. D., Allende Prieto, C., et al. 2015, *ApJS*, 219, 12
 Albareti, F. D., Allende Prieto, C., Almeida, A., et al. 2018, *ApJS*, 233, 25
 Alexandroff, R., Strauss, M. A., Greene, J. E., et al. 2013, *MNRAS*, 435, 3306

Allen, J. T., Hewett, P. C., Maddox, N., Richards, G. T., & Belokurov, V. 2011, *MNRAS*, 410, 860
 Bautista, J. E., Busca, N. G., Guy, J., et al. 2017, *A&A*, 603, A12
 Becker, R. H., White, R. L., & Helfand, D. J. 1995, *ApJ*, 450, 559
 Blanton, M. R., Bershad, M. A., Abolfathi, B., et al. 2017, *AJ*, 154, 28
 Boller, T., Freyberg, M. J., Trümper, J., et al. 2016, *A&A*, 588, A103
 Bolton, A. S., Schlegel, D. J., Aubourg, É., et al. 2012, *AJ*, 144, 144
 Bovy, J., Hennawi, J. F., Hogg, D. W., et al. 2011, *ApJ*, 729, 141
 Bovy, J., Myers, A. D., Hennawi, J. F., et al. 2012, *ApJ*, 749, 41
 Boyle, B. J., Shanks, T., & Peterson, B. A. 1988, *MNRAS*, 235, 935
 Clerc, N., Merloni, A., Zhang, Y.-Y., et al. 2016, *MNRAS*, 463, 4490
 Croom, S. M., Smith, R. J., Boyle, B. J., et al. 2004, *MNRAS*, 349, 1397
 Cutri, R. M., Skrutskie, M. F., van Dyk, S., et al. 2003, *VizieR Online Data Catalog: II/246*
 Dawson, K. S., Schlegel, D. J., Ahn, C. P., et al. 2013, *AJ*, 145, 10
 Dawson, K. S., Kneib, J.-P., Percival, W. J., et al. 2016, *AJ*, 151, 44
 Diamond-Stanic, A. M., Fan, X., Brandt, W. N., et al. 2009, *ApJ*, 699, 782
 du Mas des Bourboux, H., Le Goff, J.-M., Blomqvist, M., et al. 2017, *A&A*, 608, A130
 Dwelly, T., Salvato, M., Merloni, A., et al. 2017, *MNRAS*, 469, 1065
 Eftekharzadeh, S., Myers, A. D., White, M., et al. 2015, *MNRAS*, 453, 2779
 Eisenstein, D. J., Weinberg, D. H., Agol, E., et al. 2011, *AJ*, 142, 72
 Fan, X., Strauss, M. A., Richards, G. T., et al. 2006, *AJ*, 131, 1203
 Fathivavari, H., Petitjean, P., Zou, S., et al. 2017, *MNRAS*, 466, L58
 Filiz Ak, N., Brandt, W. N., Hall, P. B., et al. 2012, *ApJ*, 757, 114
 Filiz Ak, N., Brandt, W. N., Hall, P. B., et al. 2013, *ApJ*, 777, 168
 Filiz Ak, N., Brandt, W. N., Hall, P. B., et al. 2014, *ApJ*, 791, 88
 Finkbeiner, D. P., Schlafly, E. F., Schlegel, D. J., et al. 2016, *ApJ*, 822, 66
 Finley, H., Petitjean, P., Pâris, I., et al. 2013, *A&A*, 558, A111
 Fukugita, M., Ichikawa, T., Gunn, J. E., et al. 1996, *AJ*, 111, 1748
 Gibson, R. R., Brandt, W. N., Schneider, D. P., & Gallagher, S. C. 2008, *ApJ*, 675, 985
 Gibson, R. R., Jiang, L., Brandt, W. N., et al. 2009, *ApJ*, 692, 758
 Gunn, J. E., Carr, M., Rockosi, C., et al. 1998, *AJ*, 116, 3040
 Gunn, J. E., Siegmund, W. A., Mannery, E. J., et al. 2006, *AJ*, 131, 2332
 Hall, P. B., Anderson, S. F., Strauss, M. A., et al. 2002, *ApJS*, 141, 267
 Hamann, F., Zakamska, N. L., Ross, N., et al. 2017, *MNRAS*, 464, 3431
 Hennawi, J. F., Strauss, M. A., Oguni, M., et al. 2006, *AJ*, 131, 1
 Hewett, P. C., & Wild, V. 2010, *MNRAS*, 405, 2302 (HW10)
 Hewett, P. C., Foltz, C. B., & Chaffee, F. H. 1995, *AJ*, 109, 1498
 Hogg, D. W., Finkbeiner, D. P., Schlegel, D. J., & Gunn, J. E. 2001, *AJ*, 122, 2129
 Ivezić, Ž., Lupton, R. H., Schlegel, D., et al. 2004, *Astron. Nachr.*, 325, 583
 Jiang, L., Fan, X., Annis, J., et al. 2008, *AJ*, 135, 1057
 Kaiser, N., Aussel, H., Burke, B. E., et al. 2002, in *Survey and Other Telescope Technologies and Discoveries*, eds. J. A. Tyson, & S. Wolff, Society of Photo-Optical Instrumentation Engineers, *SPIE Conf. Ser.*, 4836, 154
 Kaiser, N., Burgett, W., Chambers, K., et al. 2010, *Society of Photo-Optical Instrumentation Engineers, SPIE Conf. Ser.*, 7733
 Kirkpatrick, J. A., Schlegel, D. J., Ross, N. P., et al. 2011, *ApJ*, 743, 125
 Krawczyk, C. M., Richards, G. T., Mehta, S. S., et al. 2013, *ApJS*, 206, 4
 Laher, R. R., Surace, J., Grillmair, C. J., et al. 2014, *PASP*, 126, 674
 Lang, D. 2014, *AJ*, 147, 108
 Law, N. M., Kulkarni, S. R., Dekany, R. G., et al. 2009, *PASP*, 121, 1395
 Lawrence, A., Warren, S. J., Almaini, O., et al. 2007, *MNRAS*, 379, 1599
 Lupton, R. H., Gunn, J. E., & Szalay, A. S. 1999, *AJ*, 118, 1406
 Lupton, R., Gunn, J. E., Ivezić, Z., et al. 2001, in *Astronomical Data Analysis Software and Systems X*, eds. F. R. Harnden Jr. F. A. Primi, & H. E. Payne, *ASP Conf. Ser.*, 238, 269
 MacLeod, C. L., Green, P. J., Anderson, S. F., et al. 2018, *AJ*, 155, 6
 Mainzer, A., Bauer, J., Grav, T., et al. 2011, *ApJ*, 731, 53
 Martin, D. C., Fanson, J., Schiminovich, D., et al. 2005, *ApJ*, 619, L1
 Merloni, A., Predehl, P., Becker, W., et al. 2012, *ArXiv e-prints* [[arXiv:1209.3114](https://arxiv.org/abs/1209.3114)]
 Morganson, E., Green, P. J., Anderson, S. F., et al. 2015, *ApJ*, 806, 244
 Myers, A. D., Palanque-Delabrouille, N., Prakash, A., et al. 2015, *ApJS*, 221, 27
 Oke, J. B., & Gunn, J. E. 1983, *ApJ*, 266, 713
 Osmer, P. S., & Smith, M. G. 1980, *ApJS*, 42, 333
 Padmanabhan, N., Schlegel, D. J., Finkbeiner, D. P., et al. 2008, *ApJ*, 674, 1217
 Palanque-Delabrouille, N., Yèche, C., Myers, A. D., et al. 2011, *A&A*, 530, A122
 Palanque-Delabrouille, N., Magneville, C., Yèche, C., et al. 2013, *A&A*, 551, A29
 Palanque-Delabrouille, N., Magneville, C., Yèche, C., et al. 2016, *A&A*, 587, A41
 Pâris, I., Petitjean, P., Aubourg, É., et al. 2012, *A&A*, 548, A66
 Pâris, I., Petitjean, P., Aubourg, É., et al. 2014, *A&A*, 563, A54
 Pâris, I., Petitjean, P., Ross, N. P., et al. 2017, *A&A*, 597, A79
 Pier, J. R., Munn, J. A., Hindsley, R. B., et al. 2003, *AJ*, 125, 1559

- Predehl, P., Andritschke, R., Böhringer, H., et al. 2010, in *Space Telescopes and Instrumentation 2010: Ultraviolet to Gamma Ray*, Proc. SPIE, 7732, 77320U
- Rau, A., Kulkarni, S. R., Law, N. M., et al. 2009, *PASP*, 121, 1334
- Reichard, T. A., Richards, G. T., Schneider, D. P., et al. 2003, *AJ*, 125, 1711
- Reyes, R., Zakamska, N. L., Strauss, M. A., et al. 2008, *AJ*, 136, 2373
- Richards, G. T., Fan, X., Newberg, H. J., et al. 2002, *AJ*, 123, 2945
- Richards, G. T., Nichol, R. C., Gray, A. G., et al. 2004, *ApJS*, 155, 257
- Richards, G. T., Strauss, M. A., Fan, X., et al. 2006, *AJ*, 131, 2766
- Rosen, S. R., Webb, N. A., Watson, M. G., et al. 2016, *A&A*, 590, A1
- Ross, N. P., Myers, A. D., Sheldon, E. S., et al. 2012, *ApJS*, 199, 3
- Ross, N. P., McGreer, I. D., White, M., et al. 2013, *ApJ*, 773, 14
- Ross, N. P., Hamann, F., Zakamska, N. L., et al. 2015, *MNRAS*, 453, 3932
- Ruan, J. J., Anderson, S. F., Green, P. J., et al. 2016, *ApJ*, 825, 137
- Schlafly, E. F., & Finkbeiner, D. P. 2011, *ApJ*, 737, 103
- Schlafly, E. F., Finkbeiner, D. P., Jurić, M., et al. 2012, *ApJ*, 756, 158
- Schmidt, M. 1963, *Nature*, 197, 1040
- Schmidt, M., & Green, R. F. 1983, *ApJ*, 269, 352
- Schneider, D. P., Hall, P. B., Richards, G. T., et al. 2007, *AJ*, 134, 102
- Schneider, D. P., Richards, G. T., Hall, P. B., et al. 2010, *AJ*, 139, 2360
- Shen, Y., Strauss, M. A., Oguri, M., et al. 2007, *AJ*, 133, 2222
- Shen, Y., Brandt, W. N., Denney, K. D., et al. 2016, *ApJ*, 831, 7
- Skrutskie, M. F., Cutri, R. M., Stiening, R., et al. 2006, *AJ*, 131, 1163
- Smee, S. A., Gunn, J. E., Uomoto, A., et al. 2013, *AJ*, 146, 32
- Smith, J. A., Tucker, D. L., Kent, S., et al. 2002, *AJ*, 123, 2121
- Spergel, D. N., Verde, L., Peiris, H. V., et al. 2003, *ApJS*, 148, 175
- Storrie-Lombardi, L. J., McMahon, R. G., Irwin, M. J., & Hazard, C. 1996, *ApJ*, 468, 121
- Stoughton, C., Lupton, R. H., Bernardi, M., et al. 2002, *AJ*, 123, 485
- Trump, J. R., Hall, P. B., Reichard, T. A., et al. 2006, *ApJS*, 165, 1
- Tucker, D. L., Kent, S., Richmond, M. W., et al. 2006, *Astron. Nachr.*, 327, 821
- Voges, W., Aschenbach, B., Boller, T., et al. 1999, *A&A*, 349, 389
- Voges, W., Aschenbach, B., Boller, T., et al. 2000, *IAU Circ.*, 7432, 3
- Weymann, R. J., Morris, S. L., Foltz, C. B., & Hewett, P. C. 1991, *ApJ*, 373, 23
- Wright, E. L., Eisenhardt, P. R. M., Mainzer, A. K., et al. 2010, *AJ*, 140, 1868
- Yèche, C., Petitjean, P., Rich, J., et al. 2010, *A&A*, 523, A14
- York, D. G., Adelman, J., Anderson Jr., J. E., et al. 2000, *AJ*, 120, 1579
- ⁷ Department of Astronomy, Box 351580, University of Washington, Seattle, WA 98195, USA
- ⁸ CEA, Centre de Saclay, IRFU, 91191 Gif-sur-Yvette, France
- ⁹ Department of Physics and Astronomy, University of Utah, 115 S. 1400 E., Salt Lake City, UT 84112, USA
- ¹⁰ Center for Cosmology and Particle Physics, Department of Physics, New York University, 726 Broadway, Room 1005, New York, NY 10003, USA
- ¹¹ Apache Point Observatory, P.O. Box 59, Sunspot, NM 88349, USA
- ¹² Department of Astronomy and Astrophysics, Eberly College of Science, The Pennsylvania State University, 525 Davey Laboratory, University Park, PA 16802, USA
- ¹³ Institute for Gravitation and the Cosmos, The Pennsylvania State University, University Park, PA 16802, USA
- ¹⁴ Department of Physics, The Pennsylvania State University, University Park, PA 16802, USA
- ¹⁵ Max-Planck-Institut für Extraterrestrische Physik, Gießenbachstr. 1, 85748 Garching, Germany
- ¹⁶ Sorbonne Universités, Institut Lagrange de Paris (ILP), 98 bis boulevard Arago, 75014 Paris, France
- ¹⁷ Laboratoire de Physique Nucléaire et de Hautes Énergies, Université Pierre et Marie Curie, 4 Place Jussieu, 75005 Paris, France
- ¹⁸ Harvard-Smithsonian Center for Astrophysics, 60 Garden St., Cambridge, MA 02138, USA
- ¹⁹ Department of Physics and Astronomy, York University, 4700 Keele St., Toronto, ON M3J 1P3, Canada
- ²⁰ Institute of Physics, Laboratory of Astrophysics, École Polytechnique Fédérale de Lausanne (EPFL), Observatoire de Sauverny, 1290 Versoix, Switzerland
- ²¹ Space Telescope Science Institute, 3700 San Martin Drive, Baltimore, MD 21218, USA
- ²² Steward Observatory, The University of Arizona, 933 North Cherry Avenue, Tucson, AZ 85721-0065, USA
- ²³ Institute of Cosmology & Gravitation, University of Portsmouth, Dennis Sciama Building, Portsmouth PO1 3FX, UK
- ²⁴ Center for Cosmology and AstroParticle Physics, The Ohio State University, 191 W. Woodruff Ave., Columbus, OH 43210, USA
- ²⁵ Department of Physics and Astronomy, Sejong University, Seoul 143-747, Korea
- ²⁶ Department of Physics and Astronomy, Ohio University, Clippinger Labs, Athens, OH 45701, USA
- ²⁷ School of Physics and Astronomy, University of St Andrews, North Haugh, St Andrews KY16 9SS, UK
- ²⁸ National Optical Astronomy Observatory, 950 North Cherry Avenue, Tucson, AZ 85719, USA
- ²⁹ National Astronomical Observatories, Chinese Academy of Sciences, 20A Datun Road, Chaoyang District, Beijing 100012, PR China

¹ Aix Marseille Univ, CNRS, LAM, Laboratoire d'Astrophysique de Marseille, 13013 Marseille, France
e-mail: isabelle.paris@lam.fr

² Institut d'Astrophysique de Paris, UMR 7095, CNRS-UPMC, 98 bis boulevard Arago, 75014 Paris, France
e-mail: petitjean@iap.fr

³ APC, University of Paris Diderot, CNRS/IN2P3, CEA/IRFU, Observatoire de Paris, Sorbonne Paris Cité, France

⁴ Department of Physics and Astronomy, University of Wyoming, Laramie, WY 82071, USA

⁵ Instituto de Astrofísica de Canarias, 38205 La Laguna, Tenerife, Spain

⁶ Departamento de Astrofísica, Universidad de La Laguna (ULL), 38206 La Laguna, Tenerife, Spain

Appendix A**Table A.1.** Format of the binary FITS table containing DR14Q.

Column	Name	Format	Description
1	SDSS_NAME	STRING	SDSS-DR14 designation – hhmmss.ss+ddmmss.s (J2000)
2	RA	DOUBLE	Right Ascension in decimal degrees (J2000)
3	DEC	DOUBLE	Declination in decimal degrees (J2000)
4	THING_ID	INT32	Unique SDSS source identifier
5	PLATE	INT32	Spectroscopic plate number
6	MJD	INT32	Modified Julian Day of the spectroscopic observation
7	FIBERID	INT32	Spectroscopic fiber number
8	SPECTRO	STRING	SDSS or BOSS
9	Z	DOUBLE	Redshift (most robust estimate for each quasar)
10	Z_ERR	DOUBLE	Error on redshift given in Col. #9
11	SOURCE_Z	STRING	Origin of the redshift measurement in Col. #9 (VI, PIPE, AUTO, OTHER)
12	Z_VI	DOUBLE	Redshift based on visual inspection (when available)
13	Z_PIPE	DOUBLE	SDSS pipeline redshift estimate
14	Z_PIPE_ERR	DOUBLE	Error on SDSS pipeline redshift estimate
15	ZWARNING	INT32	Quality flag on SDSS pipeline redshift estimate
16	Z_PCA	DOUBLE	PCA redshift (homogeneous over the full sample)
17	Z_PCA_ERR	DOUBLE	Error on PCA redshift
18	Z_MGII	DOUBLE	Redshift of the Mg II emission line
19	BOSS_TARGET1	INT64	BOSS target selection flag for main survey
20	ANCILLARY_TARGET1	INT64	BOSS target selection flag for ancillary programs
21	ANCILLARY_TARGET2	INT64	BOSS target selection flag for ancillary programs
22	EBOSS_TARGET0	INT64	Target selection flag for the eBOSS pilot survey
23	EBOSS_TARGET1	INT64	eBOSS target selection flag
24	EBOSS_TARGET2	INT64	eBOSS target selection flag
25	N_SPEC_SDSS	INT32	Number of additional SDSS spectra
26	N_SPEC_BOSS	INT32	Number of additional BOSS spectra
27	N_SPEC	INT32	Number of additional spectra (SDSS and BOSS)
28	PLATE_DUPLICATE	INT32[51]	Spectroscopic plate number for each duplicate spectrum
29	MJD_DUPLICATE	INT32[51]	Spectroscopic MJD for each duplicate spectrum
30	FIBERID_DUPLICATE	INT32[51]	Fiber number for each duplicate spectrum
31	SPECTRO_DUPLICATE	STRING[51]	SDSS or BOSS for each duplicate spectrum
32	BI_CIV	FLOAT	BALnicity Index of C IV absorption trough (in km s^{-1})
33	ERR_BI_CIV	FLOAT	Error on the BALnicity Index of C IV trough (in km s^{-1})
34	RUN_NUMBER	INT32	SDSS Imaging Run Number of photometric measurements
35	RERUN_NUMBER	STRING	SDSS Photometric Processing Rerun Number
36	COL_NUMBER	INT32	SDSS Camera Column Number (1–6)
37	FIELD_NUMBER	INT32	SDSS Field Number
38	OBJ_ID	STRING	SDSS Object Identification Number
39	PSFFLUX	FLOAT[5]	Flux in the u, g, r, i and z bands
40	IVAR_IVAR	FLOAT[5]	Inverse variance of the u, g, r, i and z fluxes
41	PSFMAG	FLOAT[5]	PSF magnitudes in u, g, r, i and z bands
42	ERR_PSFMAG	FLOAT[5]	Error on PSF magnitudes
43	MI	FLOAT	Absolute magnitude in i band $M_i [z = 2]$ with $H_0 = 70 \text{ km s}^{-1} \text{ Mpc}^{-1}$, $\Omega_M = 0.3$, $\Omega_\Lambda = 0.7$, $\alpha_v = -0.5$
44	GAL_EXT	FLOAT[5]	Galactic extinction in the five SDSS bands (Schlafly & Finkbeiner 2011)
45	RASS_COUNTS	DOUBLE	\log RASS full band count rate (counts s^{-1})
46	RASS_COUNTS_SNR	FLOAT	S/N of the RASS count rate
47	SDSS2ROSAT_SEP	DOUBLE	SDSS-RASS separation in arcsec

Table A.1. continued.

Column	Name	Format	Description
48	FLUX_0.2_2.0keV	FLOAT	Soft (0.2–2.0 keV) X-ray flux from <i>XMM-Newton</i> expressed in $\text{erg s}^{-1} \text{cm}^{-2}$
49	FLUX_0.2_2.0keV_ERR	FLOAT	Error on soft X-ray flux from <i>XMM-Newton</i> (in $\text{erg s}^{-1} \text{cm}^{-2}$)
50	FLUX_2.0_12.0keV	FLOAT	Hard (4.5–12.0 keV) X-ray flux from <i>XMM-Newton</i> expressed in $\text{erg s}^{-1} \text{cm}^{-2}$
51	FLUX_2.0_12.0keV_ERR	FLOAT	Error on hard X-ray flux from <i>XMM-Newton</i> (in $\text{erg s}^{-1} \text{cm}^{-2}$)
52	FLUX_0.2_12.0keV	FLOAT	Total (0.2–12.0 keV) X-ray flux from <i>XMM-Newton</i> expressed in $\text{erg s}^{-1} \text{cm}^{-2}$
53	FLUX_0.2_12.0keV_ERR	FLOAT	Error on total X-ray flux from <i>XMM-Newton</i> (in $\text{erg s}^{-1} \text{cm}^{-2}$)
54	LUM_0.2_12.0keV	FLOAT	Total (0.2–12.0 keV) X-ray luminosity from <i>XMM-Newton</i> expressed in erg s^{-1}
55	SDSS2XMM_SEP	DOUBLE	SDSS- <i>XMM-Newton</i> separation in arcsec
56	GALEX_MATCHED	SHORT	GALEX match flag
57	FUV	DOUBLE	<i>fuv</i> flux (GALEX)
58	FUV_IVAR	DOUBLE	Inverse variance of <i>fuv</i> flux
59	NUV	DOUBLE	<i>nuv</i> flux (GALEX)
60	NUV_IVAR	DOUBLE	Inverse variance of <i>nuv</i> flux
61	JMAG	DOUBLE	<i>J</i> magnitude (Vega, 2MASS)
62	ERR_JMAG	DOUBLE	Error in <i>J</i> magnitude
63	JSNR	DOUBLE	<i>J</i> -band S/N
64	JRDFLAG	INT32	<i>J</i> -band photometry flag
65	HMAG	DOUBLE	<i>H</i> magnitude (Vega, 2MASS)
66	ERR_HMAG	DOUBLE	Error in <i>H</i> magnitude
67	HSNR	DOUBLE	<i>H</i> -band S/N
68	HRDFLAG	INT32	<i>H</i> -band photometry flag
69	KMAG	DOUBLE	<i>K</i> magnitude (Vega, 2MASS)
70	ERR_KMAG	DOUBLE	Error in <i>K</i> magnitude
71	KSNR	DOUBLE	<i>K</i> -band S/N
72	KRDFLAG	INT32	<i>K</i> -band photometry flag
73	SDSS2MASS_SEP	DOUBLE	SDSS-2MASS separation in arcsec
74	W1MAG	DOUBLE	<i>w1</i> magnitude (Vega, WISE)
75	ERR_W1MAG	DOUBLE	Error in <i>w1</i> magnitude
76	W1SNR	DOUBLE	S/N in <i>w1</i> band
77	W1CHI2	DOUBLE	χ^2 in <i>w1</i> band
78	W2MAG	DOUBLE	<i>w2</i> magnitude (Vega, WISE)
79	ERR_W2MAG	DOUBLE	Error in <i>w2</i> magnitude
80	W2SNR	DOUBLE	S/N in <i>w2</i> band
81	W2CHI2	DOUBLE	χ^2 in <i>w2</i> band
82	W3MAG	DOUBLE	<i>w3</i> magnitude (Vega, WISE)
83	ERR_W3MAG	DOUBLE	Error in <i>w3</i> magnitude
84	W3SNR	DOUBLE	S/N in <i>w3</i> band
85	W3CHI2	DOUBLE	χ^2 in <i>w3</i> band
86	W4MAG	DOUBLE	<i>w4</i> magnitude (Vega, WISE)
87	ERR_W4MAG	DOUBLE	Error in <i>w4</i> magnitude
88	W4SNR	DOUBLE	S/N in <i>w4</i> band
89	W4CHI2	DOUBLE	χ^2 in <i>w4</i> band
90	CC_FLAGS	STRING	WISE contamination and confusion flag
91	PH_FLAG	STRING	WISE photometric quality flag
92	SDSS2WISE_SEP	DOUBLE	SDSS-WISE separation in arcsec
93	UKIDSS_MATCHED	SHORT	UKIDSS Matched
94	YFLUX	DOUBLE	<i>Y</i> -band flux density from UKIDSS (in $\text{W m}^{-2} \text{Hz}^{-1}$)
95	YFLUX_ERR	DOUBLE	Error in <i>Y</i> -band density flux from UKIDSS (in $\text{W m}^{-2} \text{Hz}^{-1}$)
96	JFLUX	DOUBLE	<i>J</i> -band flux density from UKIDSS (in $\text{W m}^{-2} \text{Hz}^{-1}$)
97	JFLUX_ERR	DOUBLE	Error in <i>J</i> -band flux density from UKIDSS (in $\text{W m}^{-2} \text{Hz}^{-1}$)
98	HFLUX	DOUBLE	<i>H</i> -band flux density from UKIDSS (in $\text{W m}^{-2} \text{Hz}^{-1}$)

Table A.1. continued.

Column	Name	Format	Description
99	HFLUX_ERR	DOUBLE	Error in H -band flux density from UKIDSS (in $\text{W m}^{-2} \text{Hz}^{-1}$)
100	KFLUX	DOUBLE	K -band flux density from UKIDSS (in $\text{W m}^{-2} \text{Hz}^{-1}$)
101	KFLUX_ERR	DOUBLE	Error in K -band flux density from UKIDSS (in $\text{W m}^{-2} \text{Hz}^{-1}$)
102	FIRST_MATCHED	INT	FIRST matched
103	FIRST_FLUX	DOUBLE	FIRST peak flux density at 20 cm expressed in mJy
104	FIRST_SNR	DOUBLE	S/N of the FIRST flux density
105	SDSS2FIRST_SEP	DOUBLE	SDSS-FIRST separation in arcsec